VNIVERSITAT DE VALÈNCIA Facultat de Física

Máster en Física Avanzada

Especialidad en Astrofísica

Trabajo Fin de Máster

ON THE ACCRETION HISTORY OF GALAXY CLUSTERS

David Vallés Pérez

Tutora: Susana Planelles Mira
Tutor: Vicent Quilis Quilis

Curso académico 2019/2020

Abstract

Galaxy clusters are the largest and most massive gravitationally bound structures in the Universe, which continue growing through mergers and accretion of matter from the cosmic web. The physics of accretion onto these objects has important effects on both dark and baryonic matter dynamics, which will be able to be probed with forthcoming observational facilities. In this respect, Numerical Cosmology can serve as a laboratory where to test models of structure formation and baryonic physics, and provide results that will help to lead and interpret future observations. In this Master's Thesis, we aim to investigate in further detail how matter is accreted onto galaxy clusters. In the first part of the work, the most salient topics on structure formation over a cosmological background, galaxy clusters' physical and observational properties and numerical cosmology are briefly reviewed. Subsequently, we analyse the results of an Eulerian Adaptive Mesh Refinement (AMR) hydrodynamical+N-Body full-cosmological simulation of a moderate-size volume domain. We have characterised the evolutionary and accretion histories of a small sample of galaxy clusters and groups. Additionally, we have further explored the effects of accretion on the inner structure of clusters and the angular distribution of mass flows.

Abbreviations

ΛCDM Λ–Cold Dark Matter. 3, 4, 8, 24
AGN active galactic nuclei. 11, 16, 22, 25
AMR Adaptive Mesh Refinement. i, 19, 21–25, 40, 42
BAO baryon acoustic oscillations. 6
CIC Cloud-in-Cell. 18
CMB Cosmic Microwave Background. 3, 5, 6, 12
DM dark matter. 4, 5, 7–11, 13, 14, 16, 21–37, 42
FFT Fast Fourier Transform. 20, 22
FLRW Friedmann-Lamâitre-Robertson-Walker. 3, 4, 13
FoF Friends of Friends. 23
HRSC High-Resolution Shock-Capturing. 19, 21
ICM intracluster medium. 5, 7–9, 11, 12, 15, 16, 31
LSS large-scale structure. 7, 9, 43
MAH mass assembly history. 28, 29, 42
MAR mass accretion rate. 29–32, 34–36, 42
MT merger tree. 24, 26, 33
NFW Navarro, Frenk & White. 11, 24, 36
NGC Nearest Grid Cell. 18
ODE Ordinary Differential Equation. 14, 16–18, 21
P^{3}M particle-particle/particle-mesh. 20
PDE Partial Differential Equation. 14, 16, 17
PM particle-mesh. 20, 22
S-Z Sunyaev-Zel'dovich. 12
SNe supernovae explosions. 6, 16, 22, 25, 29
SO Spherical Overdensity. 23, 24, 32, 34, 38, 39, 42
SPH Smoothed-Particle Hydrodynamics. 18, 19
TSC Triangular-Shaped Cloud. 18, 22

Contents

1 Introduction

Physical Cosmology deals with the origin and the evolution of the structures in the Universe. The accepted cosmological and structure formation models, grounded on numerous observational probes, depict a hierarchical –or *bottom-up*– scenario, where larger and more massive density fluctuations collapse at later times.

Galaxy clusters occupy a special place in this hierarchy, as they are the largest objects which have had time to collapse under their own gravity and detach from the cosmic expansion. In this sense, clusters are the end product of the collapse of density fluctuations on comoving scales of $\sim 10\,\mathrm{Mpc}$, and they mark the transition between two dynamical regimes (Borgani and Kravtsov, 2011). On scales above $10\,\mathrm{Mpc}$, dynamics are solely governed by gravity, and therefore are dominated by dark matter, which accounts for most of the gravitational mass in the Universe. On smaller (galactic) scales, gas dynamics and the complexity of baryonic physics become relevant.

From this special position, galaxy clusters emerge as the crossroads of astrophysics and cosmology (Kravtsov and Borgani, 2012). The abundance and distribution of clusters keep the imprint of the initial conditions and can, therefore, be used as cosmological probes to constrain the cosmological parameters (Allen, Evrard, and Mantz, 2011). At the same time, the deep gravitational wells of clusters act as veritable astrophysical laboratories, where the complex processes of galaxy formation and evolution can be tested.

During the last four decades, the understanding of structure formation in the Universe has turned from a science of order-of-magnitude estimates to a field capable of providing really precise observations and theoretical predictions, especially due to the advent of Numerical Cosmology (Bertschinger, 1998; Dolag et al., 2008). Cosmological simulations provide a powerful tool to test the current understanding of structure formation and constrain the associated physical processes.

Despite the enormous progress in the field, important problems, mostly associated with the complex physics of baryons, remain unsolved (see, e.g., Planelles, Schleicher, and Bykov, 2015 for a recent review). In this regard, a lot of interest has been recently triggered on the role of a wide variety of phenomena associated to cosmic flows: shock waves, turbulence, mergers, accretion and the complex interplay between baryons and dark matter in such scenarios, etc. As an example, recent works have shown that accretion can impact the morphological and thermodynamical quantities of clusters and bias observational determinations of clusters' masses (H. Chen et al., 2019).

Motivated by the increasing concern of the scientific community on these phenomena, the main aim of this work is to provide a general introduction to the physics of galaxy clusters and the techniques of Numerical Cosmology, and to apply them in order to quantitatively analyse how matter is accreted onto galaxy clusters in a cosmological environment. To achieve this last point, several analyses have been conducted on the outputs of a full-cosmological simulation, providing results that are consistent with the previous literature and adding some insight on several topics not yet extensively covered.

1.1 Organisation of the manuscript

In Sec. 2, the theoretical background for this work is briefly reviewed. This includes an introduction to the currently accepted cosmological model (Sec. 2.1) and the physical and observational properties of galaxy clusters (Sec. 2.2 and 2.3, respectively).

A summary on the modelling of the evolution of inhomogeneities in the Universe and the numerical tools that are employed in order to track this evolution is presented in Sec. 3, and the specific tools used in this work are described in Sec. 4.

In Sec. 5, the results of our analyses on the outputs of a cosmological simulation are presented in several subsections. Through them, we highlight their physical interpretation but also carefully describe the implemented methods and discuss the underlying assumptions.

Finally, in Sec. 6, we summarise the main findings and conclusions of this work and point out several continuation lines of these analyses.

2 | Galaxy Clusters in a Cosmological Environment

In Sec. 1, the special place of galaxy clusters in the cosmic hierarchy has already been motivated, both because of them being the largest objects which have had time to gravitationally collapse and because of their implications as cosmological probes and astrophysical laboratories. In Sec. 2.1, the main ingredients for the description of the cosmological background upon which clusters form are introduced. The most relevant physical and observational properties of these vast structures are subsequently discussed in Sec. 2.2 and 2.3, respectively.

2.1 Structure formation over a cosmological background

Structure formation through the history of the Universe is determined by the initial conditions and by a cosmological model, which together shape the properties and evolution of the Universe (Planelles, Schleicher, and Bykov, 2015). Currently, the accepted cosmological paradigm is the ΛCDM or *concordance* model, also labelled as the *standard model of cosmology* by some authors (Hamilton, 2014). The acronym stands for dark energy (Λ) and cold dark matter (CDM). Through the following pages, a succinct overview of the model is presented. First, the *background* Universe will be motivated and introduced. Then, deviations from such background, which ultimately lead to the observed cosmic structure, are considered.

2.1.1 A Universe of mean values

The background model of the Universe is that of a homogeneous and isotropic system. The former means that the Universe looks –statistically– the same when seen from any point, while the latter implies that it presents equivalent features in any direction. This assumption is commonly named the *Cosmological Principle*. Its motivation is, at least, twofold: from an operational point of view, it is the simplest physical description of such a complex system; and, even more important, when sufficiently large scales are considered, these approximations hold to a very good level of accuracy[1]. Far from being a groundless hypothesis, numerous cosmological probes support it. Without entering into further detail, we can mention the distribution of distant galaxies in large-scale surveys (e.g. SDSS, 2dF) and the extreme isotropy of the Cosmic Microwave Background (CMB) temperature field, which holds down to roughly a part in 10^5. A more thorough review of probes supporting the Cosmological Principle can be found in Hamilton (2014).

Under the assumptions of homogeneity and isotropy, the mathematical description of the geometry of space-time is the Friedmann-Lamâitre-Robertson-Walker (FLRW) metric, which can be given in spherical coordinates adapted to the cosmological observer ($u \equiv \partial_t$) by the arc element:

[1] Such a characteristic length to regard the Universe as homogeneous can be established in the order of $\sim 100\,\mathrm{Mpc}$ (Ntelis, 2016). Below this scale, gravity and other physical processes have produced the collapse of structures, naturally breaking both homogeneity and isotropy.

$$\mathrm{d}s^2 = -\mathrm{d}t^2 + a(t)^2 \left(\frac{\mathrm{d}r^2}{1-kr^2} + r^2 \mathrm{d}\theta^2 + r^2 \sin^2\theta \mathrm{d}\phi^2 \right), \tag{2.1}$$

where k is the –constant– scalar curvature of FLRW space-time and $a(t)$ is the scale factor. The scalar curvature can only take the values $k = -1$, 0, $+1$, corresponding to open, flat and closed universes, respectively. The scale factor, $a(t)$, accounts for the cosmic expansion. In a flat ($k = 0$) Universe, the scale factor can be normalised so that $a(t = t_0) \equiv a_0 = 1$, where t_0 stands for the present time. A radial distance $D_\mathrm{c} \equiv \int \mathrm{d}r$ will be referred to as a *comoving distance*, while the proper length $\int a(t)\mathrm{d}r$ will be regarded as the *physical distance*.

The dynamical description of such an isotropic and homogeneous background universe is complete once $a(t)$ is known. In order to do so, one needs to solve Einstein equations, $G_{\mu\nu} + \Lambda g_{\mu\nu} = \frac{8\pi G}{c^4} T_{\mu\nu}$, being $G_{\mu\nu}$ the Einstein tensor (depending on the metric tensor, $g_{\mu\nu}$, and its space-time derivatives up to second order), Λ the cosmological constant and $T_{\mu\nu}$ the energy-momentum tensor. The cosmological fluid is assumed to be a perfect fluid, and hence its energy-momentum tensor can be written as $T_{\mu\nu} = \left(\rho_B + \frac{p_B}{c^2}\right) u_\mu u_\nu + p_B g_{\mu\nu}$, being ρ_B the density of the cosmic fluid, p_B its pressure and u^μ its 4-velocity. Using this explicit form for the energy-momentum tensor and the FLRW metric, Einstein equations yield two independent equations for the three unknowns (namely $a(t)$, ρ_B and p_B). These equations can be rearranged to yield Friedmann equations in their most usual form (Peebles, 1993):

$$\left(\frac{\dot{a}(t)}{a(t)}\right)^2 = \frac{8\pi G}{3}\rho_\mathrm{B}(t) + \frac{\Lambda}{3} - \frac{kc^2}{a(t)^2} \tag{2.2}$$

$$\dot{\rho}_\mathrm{B} + 3\frac{\dot{a}}{a}\left(\rho_\mathrm{B} + \frac{p_\mathrm{B}}{c^2}\right) = 0 \tag{2.3}$$

To solve the system, an equation of state for the background is required to eliminate one of the variables. In cosmology, the equation of state is often written as[2] $p_B = w\rho_B c^2$. Different components of the Universe have different equations of state, i.e., different values of the dimensionless parameter w.

The ΛCDM cosmological model is a particularisation of the FLRW models, with a well-defined selection of the components of the Universe (Hamilton, 2014). These are:

- Almost 70% of the energy content of the Universe is in the form of an elusive *Dark Energy* component, whose fundamental nature remains yet unknown. It drives the accelerated expansion of the Universe and is consistent with a cosmological constant (Λ) term in Eq. (2.2). Hence, its equation of state is $w = -1$.

- Roughly 25% of the Universe is composed of some kind of gravitational matter which cannot be electromagnetically detected: the so-called *dark matter (DM)*. Although its fundamental nature is not yet understood, it certainly interacts very little with baryonic matter (besides gravitationally). It is assumed to be

[2] As an abuse of terminology, the parameter w by itself is often referred to as «the equation of state» of the species.

cold, i.e., non-relativistic and hence pressureless, ($w = 0$). By not feeling the electromagnetic interaction (and thus being a *collisionless* component), DM was allowed to collapse before regular matter did, creating DM haloes which would then lead to the formation of galaxies and larger structures (Bertschinger, 1998).

- Only around 5% of the energy budget is due to regular, *baryonic* matter, forming the stars and gas clouds that can be directly detected. Most of this matter is in the form of a hot thermal plasma, observable in the X-Ray band, filling galaxy clusters: the intracluster medium (ICM). Cold baryons, the ones giving rise to structures like stars and galaxies, only account for around a quarter of the total regular matter content. The physics of this apparently subdominant material component is fundamental to provide a faithful description of the formation of the structures in the Universe (Planelles, Schleicher, and Bykov, 2015).

Radiation components are completely negligible in the present Universe, but they were dominant during the first tens of thousands of years. By being relativistic species, with $w = \frac{1}{3}$, Eq. (2.3) predicts a faster decline in their densities, scaling as $\rho_B \propto a^{-4}$ (instead of $\rho_B \propto a^{-3}$ for cold matter).

2.1.2 Inhomogeneities in the Universe

Up to this point, a Universe of homogeneous, background quantities has been described. This model settles the bases upon which structure formation occurs. The seeds for this cosmological structure formation are the tiny fluctuations that appear imprinted on the CMB temperature field (with a rms relative amplitude in the order of $\sim 10^{-5}$), which correspond to density fluctuations of the same order in the surface of last scattering.

The origin of these fluctuations, however, traces back to a much more primordial Universe: they are thought to have appeared during the inflationary era, a period of accelerated expansion in the very early Universe, which solves several open problems in early-Universe cosmology (Peebles, 1993; Tanabashi et al., 2018, §22). After the decoupling of radiation and matter ($z_{\rm dec} \approx 1100$), these perturbations grow hierarchically, forming larger and more massive structures at later times. The mathematical description of the evolution of such inhomogeneities is left to be discussed in more detail in Sec. 3.1.

2.1.3 Cosmological parameters

From Eq. (2.2), the density of a flat ($k = 0$) universe with no cosmological constant ($\Lambda = 0$) can be obtained. This density is known as the *critical density*, and its value equates to $\rho_c(t) = \frac{3H(t)^2}{8\pi G}$, where $H(t) \equiv \frac{\dot{a}}{a}$ is the Hubble parameter. The matter density can be split in its baryonic and DM contributions, $\rho_m(t) = \rho_b(t) + \rho_{\rm DM}(t)$. The cosmological constant can be assigned a density as well, by defining $\rho_\Lambda = \frac{\Lambda}{8\pi G}$.

These densities are often given in terms of their corresponding density parameters, $\Omega_X \equiv \frac{\rho_{X0}}{\rho_{c0}}$, where X stands for any of the considered species and the subindex 0 indicates that the quantities are measured in the present. It is customary to define

TABLE 1: Latest values reported by Planck Collaboration (2018) of the most relevant cosmological parameters.

Name	Symbol	Value
Density parameter of baryonic matter[3]	Ω_b	0.04897 ± 0.00068
Density parameter of matter	Ω_m	0.3111 ± 0.0056
Density parameter of dark energy	Ω_Λ	0.6889 ± 0.0056
Hubble dimensionless parameter	h	0.6766 ± 0.0044
Index of the power spectrum	n_s	0.9665 ± 0.0038
Amplitude of the power spectrum	$10^9 A_s$	2.105 ± 0.030
Age of the Universe[4]	t_0	13.787 ± 0.020 Gyr

a curvature density parameter as $\Omega_k = -H_0^2 \frac{kc^2}{a_0^2}$. It is easy to see that Eq. (2.2) is then rewritten as $1 = \Omega_m + \Omega_\Lambda + \Omega_k$. The previously mentioned $k = -1,\ 0,\ +1$ cases correspond to $\Omega_m + \Omega_\Lambda <, =, > 1$, respectively. Ω_m, Ω_b and Ω_Λ (or any combination) are, therefore, fundamental parameters of the cosmological model.

Another relevant quantity is the Hubble constant (the value of Hubble parameter in the present, $H_0 \equiv H(t_0)$), usually given via the *dimensionless Hubble constant* $h \equiv \frac{H_0}{100\,\mathrm{km/s/Mpc}}$. Further parameters that we may introduce without too much depth are the amplitude, A_s, and spectral index, n_s, of the power spectrum of the primordial density fluctuations ($P(k) = A_s k^{n_s}$), which fully determine the statistical properties of the initial conditions for structure formation. Some additional quantities, like the optical depth of reionisation, τ, are not intrinsically fundamental, but are not currently derivable from the former ones with a good level of accuracy, and are added as free parameters instead (Liddle, 2004).

Determining the cosmological parameters is a non-trivial task, since most of the times individual probes can only provide constraints among different parameters, up to some degeneracy. In order to effectively constrain all the parameters, statistical analyses are performed combining the confidence regions in the parameter space for a variety of different probes (see, e.g., Planck Collaboration, 2018). Amongst the many cosmological probes, we can count the observation of standard candles (like supernovae explosions (SNe) of type Ia), primary anisotropies in the CMB (like the ones due to baryon acoustic oscillations (BAO)), galaxy clustering, weak gravitational lensing, etc. (recent reviews can be found in Hamilton, 2014; Tanabashi et al., 2018, §24). The latest values of these parameters, as reported by Planck Collaboration (2018), are shown in Table 1.

2.2 Physical properties of galaxy clusters

In Sec. 1, the special place of galaxy clusters as crossroads of cosmology and astrophysics has been introduced. Through the following pages, the main physical properties of these objects are briefly reviewed. Most of the topics mentioned here

[3] Ω_b is not explicitly given in Planck Collaboration (2018). Instead, $\Omega_\mathrm{b} h^2$ is. The value of Ω_b presented here has been obtained using the value of h; and its error has been estimated using the error propagation formula and assuming no correlations.

[4] Although this is not a free parameter (as it can be easily computed from the ones above), it is added for the sake of completeness.

are covered in further detail in recent reviews, like Borgani and Kravtsov (2011); Kravtsov and Borgani (2012); Planelles, Schleicher, and Bykov (2015); Walker et al. (2019).

2.2.1 General features of clusters

Galaxy clusters are the largest and most massive gravitationally bound structures in the Universe. Typical masses for these objects lie in the range of 10^{14} to $10^{15}\,M_\odot$. Their spatial extension can reach a few Mpc, and the largest ones contain up to thousands of galaxies. Aggregations of a small number of galaxies (in the order of tens), with masses around $10^{13} M_\odot$ and radii of $\sim 1\,\mathrm{Mpc}$, are called *groups*. Nevertheless, there is not a well-defined boundary between groups and galaxy clusters. Clusters are interconnected amongst themselves through a network of filaments and walls, which are characteristic of the large-scale structure (LSS), with typical separations of tens of Mpc (Borgani and Kravtsov, 2011).

Despite the previous description, stars and gas in galaxies only account for a few percents of the clusters' masses. The bulk of baryonic matter in galaxy clusters is in the form of a hot, thermal, fully-ionised plasma: the ICM. Typical particle number densities in such plasma range between 10^{-1} and $10^{-4}\,\mathrm{cm}^{-3}$. The emission properties of this ICM will be covered in more detail in Sec. 2.3. Yet including this diffuse component, baryons only make for around $15-20\%$ of the mass in clusters. The rest corresponds to DM, which was already found in these cosmic structures by Zwicky (1933) almost a century ago.

The abundance of gas, stars and baryons in cosmic structures is often quantified in the bibliography (e.g., Planelles et al., 2013) through their respective fractions, f_g, f_* and f_b:

$$f_g \equiv \frac{M_g}{M_{\mathrm{tot}}}, \qquad f_* \equiv \frac{M_*}{M_{\mathrm{tot}}}, \qquad f_b \equiv f_g + f_*, \tag{2.4}$$

where $M_{\mathrm{tot}} = M_g + M_* + M_{\mathrm{DM}}$. In these fractions, the masses are measured inside some defined radius, according to the definitions that will be introduced in Sec. 2.2.2. Although these quantities present important uncertainties, both in simulations and observations, as a general trend[5] baryons account for a mass fraction $f_b \sim 0.15$ for a fairly wide mass interval. The stellar fraction depends noticeably on cluster's mass, decreasing from $f_* \sim 0.05$ for $10^{14} M_\odot$ to $f_* \sim 0.03$ for $10^{15} M_\odot$. However, these values are strongly dependent on the physics of baryons and, therefore, huge uncertainties regarding their determination remain present.

The shape of galaxy clusters is mostly determined by the shape of the DM halo which gives rise to it. The simplest models for the collapse of density perturbations on cosmic scales assume these haloes to be spherical (e.g., the *top-hat* model; Gunn and Gott, 1972). However, since the 1980s, N-Body and, more recently, hydrodynamical simulations have shown that they are generally triaxial (Bertschinger, 1998; Kravtsov and Borgani, 2012). The major axis is generally aligned with the filament connecting the cluster to its nearest massive neighbour, as mergers preferentially occur along this direction (Lee and Evrard, 2007; Kravtsov and Borgani, 2012).

[5] The quantities presented here, taken from Planelles et al. (2013), are measured inside R_{500c}. This definition of radius is presented in Sec. 2.2.2.

Closely connected to shape, it is worth mentioning the dynamical state of clusters. Virial (for the dark component) and/or hydrostatic equilibrium (for the gas) are common assumptions in order to observationally estimate the mass of clusters. After its collapse, an isolated cluster would gradually relax to an equilibrium state. However, hydrodynamical simulations have recently pointed out significant departures from that equilibrium (Biffi et al., 2016). Mergers are an important source of energetic feedback, as they transform gravitational energy to thermal energy (Planelles and Quilis, 2009). Mergers and smooth accretion onto galaxy clusters impact the dynamical state of clusters, and the overall accretion phenomena correlate with the ellipticity of the ICM (H. Chen et al., 2019).

2.2.2 Masses and radii definitions

Even though the shape of DM haloes and their baryonic counterpart, the ICM, is generally triaxial, in the literature it is customary to measure the mass distribution in spherically averaged profiles (Kravtsov and Borgani, 2012). Despite this simplification, defining clusters' radii and masses is not a trivial issue, due to the absence of any well-defined boundary.

The most common practice in the clusters' studies is to set a boundary defined by a radius, R_Δ, which encloses a mean overdensity Δ with respect to some reference density, $\rho_{\rm ref}$. Usual reference densities are either the critical density of the Universe, $\rho_c(z)$, or the background matter density, $\rho_B(z) = \Omega_m(z)\rho_c(z)$. Note, however, that these two densities evolve differently with redshift. While $\rho_B(z) = \rho_{B0}(1+z)^3$, as derived from Eq. (2.3), $\rho_c(z) = \rho_{c0}E(z)^2$, where $E(z) = \frac{H(z)}{H_0} = \sqrt{\Omega_m(1+z)^3 + \Omega_\Lambda}$ for a ΛCDM cosmology. In any case, with these definitions, the radius, R_Δ, and its corresponding mass, $M_\Delta = M(< R_\Delta)$, can be simultaneously found by solving the integral equation

$$M_{\Delta_c} = \frac{4\pi}{3}\Delta_c\rho_c(z)R^3_{\Delta_c} \qquad \text{or} \qquad M_{\Delta_m} = \frac{4\pi}{3}\Delta_m\rho_B(z)R^3_{\Delta_m}. \tag{2.5}$$

For instance, the most recent X-Ray observations with Chandra or XMM-Newton can accurately resolve the density and temperature profiles of clusters inside R_{500c} (Walker et al., 2019). In simulations, many works choose R_{200m} as the boundary of the cluster (e.g., H. Chen et al., 2019), but this election is, to some extent, arbitrary and there is not a unique criterion for defining cluster boundaries in the literature.

Motivated by the spherical collapse model, another widely used physical scale of clusters is the virial radius. This radius is obtained from the study of the collapse of a homogeneous, spherically symmetric overdensity in an expanding universe. In an Einstein-de Sitter cosmology ($\Omega_m = 1$, $\Omega_\Lambda = 0$), this radius corresponds to an overdensity $\Delta_{\rm vir,c} = 18\pi^2 \approx 178$. In a flat, ΛCDM cosmology ($\Omega_m + \Omega_\Lambda = 1$), the virial overdensity can be approximated by (Bryan and Norman, 1998):

$$\Delta_{\rm vir,c} = 18\pi^2 + 82x - 39x^2 \tag{2.6}$$

where $x = \Omega_m(z) - 1$ and $\Omega_m(z) = \Omega_m\frac{(1+z)^3}{E(z)^2}$. For example, for the parameters given in Table 1, $\Delta_{\rm vir,c} \approx 103$ and $\Delta_{\rm vir,m} \approx 330$ at $z = 0$.

Last, let us introduce two additional radii definitions for the sake of completeness. Recent works (More, Diemer, and Kravtsov, 2015) show that a natural boundary for

DM haloes can be defined by considering the apocenter of DM particles' orbits after their first infall to the cluster. This process is reflected as a sharp drop in density profiles, from which the *splashback radius*, $R_{\rm sp}$, can be measured. As for the baryonic component, as low-density matter is accreted, an external shock (the *accretion shock*) is formed. This shock radius, $R_{\rm sh}$, can be regarded as a physical boundary of the gaseous component. Typical orders of magnitude of the aforementioned radii yield an approximate relation $R_{500c} : R_{200m} : R_{\rm sp} : R_{\rm sh} = 1 : 3 : 4 : 6$ (Walker et al., 2019), although this depends on the inner structure of the objects.

2.2.3 Formation of clusters

Formation and evolution of galaxy clusters is an active topic of research. While some areas are well understood, either via theoretical models or numerical simulations, important uncertainties remain, especially those due to the physics of galaxy formation and feedback. Here, we shall only present a succinct overview of the most general features of galaxy cluster formation, while more detailed reviews can be found in Kravtsov and Borgani (2012); Planelles, Schleicher, and Bykov (2015).

Current understanding of structure formation in the Universe favours a hierarchical (or *bottom-up*) scenario, in which larger and more massive structures form at later stages. This evolution is mainly governed by gravity, through a series of mergers and accretion of smaller systems. In this respect, clusters occupy a special position in the cosmic hierarchy, as they are the largest structures which have had time to collapse (Borgani and Kravtsov, 2011).

The gravitational collapse of such structures is primarily driven by the dark component: DM starts collapsing at early redshifts, creating a complex network of cosmic filaments. Massive haloes are usually located at the intersections of such filaments, resulting in deep potential wells which will give rise to clusters. These potential wells get deeper as haloes undergo mergers and accrete smaller systems, mainly through the cosmic filaments. The gaseous component roughly traces the shape of the DM halo, although its collisional nature (as opposed to the collisionless nature of DM) makes the gas distribution smoother due to the pressure support. Regions which are dense enough and can cool efficiently start forming stars since relatively early redshifts. Thus, the distribution of stars is more clumpy than its gaseous counterpart. As a realisation of this, Fig. 1 presents the evolution of DM, gas and stellar densities for four redshifts in a cosmological simulation.

Due to the large masses involved in the process of cluster formation, these events are amongst the most energetic ones in the history of the Universe (involving energies up to 10^{65} erg; Borgani and Kravtsov, 2011). The strong gravitational field of the forming cluster can accelerate both, dark and baryonic matter, to high speeds (in the order of ~ 1000 km/s). Gas flows soon become supersonic, giving rise to shock waves, which are ubiquitous in the process of cluster formation. These shocks play an important role in thermalizing and reheating the ICM, as they convert kinetic energy into internal energy (Planelles and Quilis, 2013).

Cluster formation is a process extended in time (with timescales in the order of Gyr), maintained by frequent mergers and accretion. The accretion pattern is complex, resulting in aspherical shocks. Most of the accretion of gas takes place around the LSS filaments, where the surrounding gas has higher density and lower temper-

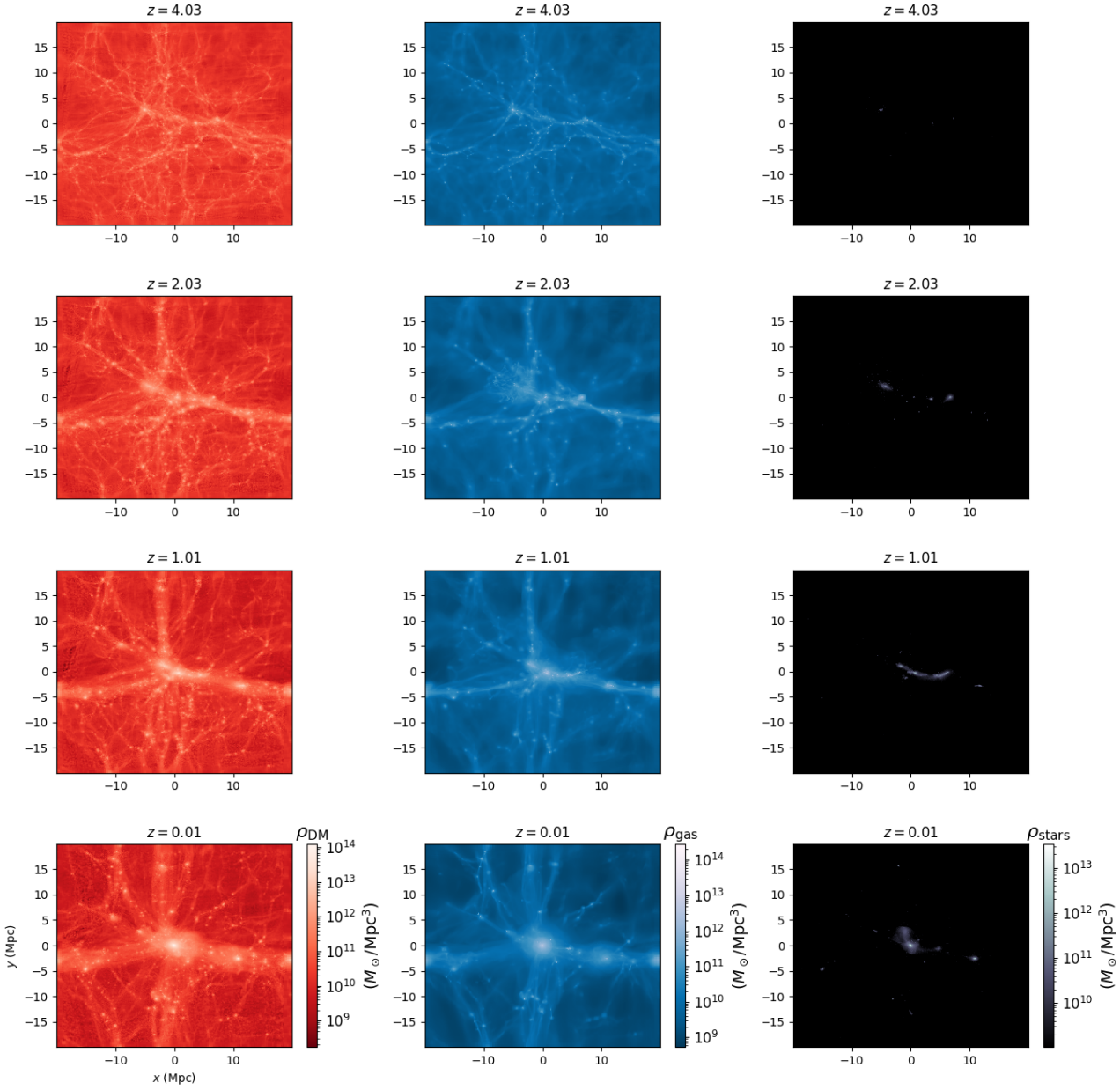

FIGURE 1: Evolution of the DM density (left), gas density (central) and stellar density (right), at $z = 4$, 2, 1 and 0 (from top to bottom), from the cosmological simulation presented in Sec. 4.3. Each panel is a projection along the third axis, for the central 10 comoving Mpc. x and y coordinates are comoving (the side of the box is 40 Mpc at $z = 0$). The colour scale shown at the bottom of each column applies to each panel in the column.

ature (and therefore lower entropy). Thus, accretion to galaxy clusters turns out to be a complex process, due to the interaction of the system with its surroundings.

2.2.4 Inner structure

During the 1990s, an important effort was devoted to study the structure of collapsed DM haloes from N-Body simulations. As a result, Navarro, Frenk, and

White (1997) found a universal density profile for DM haloes, characterised by a gradual steepening of the profile from $\rho \propto r^{-1}$ at small radii to $\rho \propto r^{-3}$ at large radii. The Navarro, Frenk & White (NFW) profile is usually given as

$$\rho_{\rm NFW}(r) = \rho_c \frac{\delta_c}{(r/r_s)\,(1+r/r_s)^2}, \tag{2.7}$$

where δ_c is a characteristic density contrast and r_s is the scale radius, where the logarithmic slope of the profile is -2. Because of it being universal, as gravity does not have preferred scales, these DM density profiles are said to be self-similar. However, density profiles of the baryonic component are fairly more diverse, due to hydrodynamical phenomena and the complex physics of baryons.

The scatter in the radial profiles of several quantities (density, pressure, etc.) has been used in the bibliography to define three radial regions in galaxy clusters (Kravtsov and Borgani, 2012; Walker et al., 2019):

- Cluster cores ($r \lesssim R_{2500c}$). In these regions, thermodynamical quantities depart significantly from self-similarity. The uncertain physics of baryons (like feedback mechanisms from star evolution, active galactic nuclei (AGN), etc.) are dominant and impact importantly the thermodynamical properties of the ICM. A complete theoretical understanding has not yet been established.

- Intermediate radii ($R_{2500c} \lesssim r \lesssim R_{500c}$). These regions show the most regular behaviour. A number of scaling relations amongst different thermodynamical quantities and the mass show very small scatter in these intermediate radii. We shall not cover such scaling relations in this text, as they fall beyond the scope of the work, but their importance is crucial, both from the theoretical and the observational point of view. A recent review on the topic can be found in Giodini et al. (2013).

- Cluster outskirts ($r \gtrsim R_{500c}$). Because of instrumental limitations, these regions have not yet been extensively observed. However, the situation is likely going to change in the next decade, due to the forthcoming observational facilities. Cluster outskirts are dynamically active regions, which have suffered the effects of recent mergers and strong accretion. Departures from hydrostatic equilibrium, turbulence and clumpiness are expected to be present at these radii. These out-of-equilibrium phenomena have important effects on observational determinations of physical properties of clusters. A recent review on these clusters' regions can be found in Walker et al. (2019).

In any case, these boundaries are just approximate limits, which may vary depending on the particular study which is being performed or other instrumental limitations.

2.3 Observations of galaxy clusters

Clusters were first observed in the optical band in the late eighteenth century by astronomers Charles Messier and William Herschel. However, as already discussed in Sec. 2.2.1, the stellar component is subdominant in terms of mass. Accordingly, an important part of the emission of clusters does not come in the form of optical light,

from the stars and galaxies, but in X-Ray, from the hot ICM. In this section, the main observable bands for clusters' studies, namely optical, X-Ray and microwaves are succinctly described; while a more extensive review on the topic can be found in Voit (2005).

- In the optical band, set aside the historical observations of Messier and Herschel, some of the most influential catalogues have been the ones due to George Abell and collaborators, which contain most of the nearby galaxy clusters. Many of the optical cluster survey techniques used nowadays are extensions based on those originally developed by Abell (1958)[6]. Information about the mass and the dynamics can then confirm the true status of clusters of these candidates. One proxy for the cluster mass is its total optical luminosity. In Abell's catalogues, this is quantified in 5 categories of «optical richness», depending on the number of constituent galaxies. However, this method can suffer from projection effects. Other, more robust ways of determining the mass in optical studies are the measurement of member galaxy velocities (which allows measuring the mass using the virial theorem) and the shear distortion on background galaxies due to weak gravitational lensing.

- Galaxy clusters are powerful X-Ray emitters due to the inefficiency of galaxy formation (Voit, 2005). As already mentioned in Sec. 2.2.1, most of the baryons do not belong to any galaxy, but rather form the diffuse ICM. In general, diffuse gas is difficult to detect, unless it is compressed and heated by a deep potential well. There are two main sources of emission from such a hot gas: thermal bremsstrahlung and emission lines. The former contribution has a dependence on gas density as $L_X \propto \rho_g^2$, as can be intuitively understood from the fact that the rate of interactions depends on the probability of encounter of an ion and an electron. Typical X-Ray luminosities of clusters range $L_X \sim 10^{43} - 10^{45}\,\mathrm{erg/s}$. As for line emission, X-Ray space observatories (Chandra, XMM-Newton or, more recently, Suzaku) allow the determination of individual element abundances, provided that enough photons can be collected. On average, metallicities of clusters are around 0.3 times the solar ratios.

- In the microwave region of the electromagnetic spectrum, hot gas from clusters is observed from the effect it originates on the CMB. The main of these effects is the *thermal Sunyaev-Zel'dovich (S-Z)* effect. Inside the potential well of clusters, there is a thermal population of electrons which produce inverse Compton scattering on the CMB photons, shifting them to higher energies. Macroscopic movement of the cluster produces an additional *kinetic S-Z* effect. One important feature of this effect is the fact that it is nearly independent of the distance to the cluster. Thus, S-Z effect arises as a powerful tool to discover clusters. However, projection effects can originate confusion between different objects along the line of sight.

[6] In the original approach by Abell, once a circular region in the sky was identified as a cluster candidate, its distance was estimated from the assumption that the tenth brightest galaxy had the same absolute magnitude for all clusters. Then, the number of galaxies brighter than a limiting magnitude, set to two magnitudes fainter than the third brightest member, were counted inside a fixed radius of 2 Mpc.

3 | Numerical Simulations

In Sec. 2.1, the homogeneous and isotropic Universe has been introduced. This section deals with the mathematical description of the perturbations over this background model. The basic equations used to model the evolution of the non-linear density perturbations of both, the dark and the gaseous components, are presented in Sec. 3.1. Because of their strong nonlinearity, these equations need to be solved numerically in virtually all situations. Thus, in Sec. 3.2, the main families of numerical schemes that are employed in cosmological simulations are described.

3.1 Modelling the content of the Universe

Owing to their different nature, the gaseous and the dark components receive different mathematical treatments. The latter, because of its pressureless and collisionless nature and the fact that it only feels gravity, is studied as a set of particles which sample its phase space (see Sec. 3.1.1); while the former, by being a collisional component, can be modelled by means of a hydrodynamical treatment (Sec. 3.1.2). As already described, cold baryons (like the ones forming stars) have only a subdominant contribution, in terms of mass. Besides, the typical scales involving this component are much smaller than the ones resolved by cosmological numerical simulations. That is why they are added as phenomenological parametrisations, briefly covered in Sec. 3.1.3. Last, the initial conditions are succinctly discussed in Sec. 3.1.4.

Through all the discussion in this section, comoving coordinates will be used. The comoving (or peculiar) position is denoted[7] by $\mathbf{x}$, and the comoving velocity by $\mathbf{v} \equiv a(t)\frac{\mathrm{d}\mathbf{x}}{\mathrm{d}t}$. Note that, being the physical coordinate $\mathbf{r} = a\mathbf{x}$, the physical velocity is $\mathbf{u} \equiv \dot{\mathbf{r}} = \mathbf{v} + \dot{a}\mathbf{x}$. The additional term, $\dot{a}\mathbf{x}$, is known as the *Hubble flow*. The differential operator ∇ is also referred to derivatives with respect to the comoving coordinate.

3.1.1 Dynamics of dark matter

The direct and exact approach to solving the dynamics of any material component, DM in particular, would involve solving the Boltzmann equation for its distribution function, $f(\mathbf{x}, \mathbf{p}, t)$:

$$\frac{\partial f}{\partial \mathbf{x}}\dot{\mathbf{x}} + \frac{\partial f}{\partial \mathbf{p}}\dot{\mathbf{p}} + \frac{\partial f}{\partial t} = \left(\frac{\delta f}{\delta t}\right)_{\mathrm{col}}, \tag{3.1}$$

where the dot implies differentiation with respect to time and the right-hand side term is the *collision term*, depending on the interaction properties of the species. In the case of DM, the collision term is identically null and the resulting equation is called

[7] In Sec. 2.1, the comoving radial coordinate of the FLRW metric is denoted $r \equiv |\mathbf{x}|$, and should not be confused with the magnitude of the physical position vector, $|\mathbf{r}|$. Unfortunately, this slightly misleading notation is quite widespread in the literature (e.g., Peebles, 1993), and we keep it in order not to add further confusion. Unless explicitly staten, whenever we use a radial distance r in this text, we will be referring to a comoving distance.

Vlasov equation. In any practical application, because of the high dimensionality of the phase space, a direct numerical solution to this equation is prohibitively expensive (Borgani and Kravtsov, 2011). Instead, as it is often done with high-dimensional equations, a Monte-Carlo technique is used. The most common of these approaches are the N-Body simulations.

In these techniques, a set of N particles sample the –discretised– phase space of the DM distribution. Individual particles are evolved in time according to the Newtonian laws of motion in comoving coordinates[8], which are a set of Ordinary Differential Equations (ODEs) (Peebles, 1980):

$$\mathbf{v} = a(t)\frac{\mathrm{d}\mathbf{x}}{\mathrm{d}t} \equiv a(t)\dot{\mathbf{x}} \tag{3.2}$$

$$\frac{\mathrm{d}\mathbf{v}}{\mathrm{d}t} = -\frac{1}{a(t)}\nabla\phi - H(t)\mathbf{v} \tag{3.3}$$

In these equations, $\phi(t, \mathbf{x})$ is the *peculiar* Newtonian gravitational potential, which is defined from the usual gravitational potential (Φ) as $\phi = \Phi + \frac{1}{2}a\ddot{a}x^2$. The peculiar potential is generated by the total overdensity through the comoving Poisson's equation, which is an elliptic Partial Differential Equation (PDE),

$$\nabla^2\phi = 4\pi G a^2 \rho_B \delta_T = \frac{3}{2}H^2 a^2 \delta_T, \tag{3.4}$$

where $\delta_T \equiv \delta + \delta_* + \delta_{\mathrm{DM}} + 2$ is the total density contrast, and $\delta_i \equiv \frac{\rho_i - \rho_B}{\rho_B}$ is the density contrast of the material component i (either DM, stars, or gas; for the latter, conventionally no subindex is used). Note that only gravity couples the dark and the baryonic components.

3.1.2 Hydrodynamics in an expanding frame

The gaseous component, which constitutes the bulk of baryonic mass, is highly collisional and can be described as a non-viscous, self-gravitating fluid. Let us consider an Eulerian description and denote by $\frac{\partial}{\partial t}$ the Eulerian time derivative[9]. As it was the case for the dark component, relativistic corrections are unimportant at the scales resolved by cosmological simulations. Thus, the evolution of inhomogeneities in the gaseous component over a homogeneous and isotropic cosmological background is governed by the equations of classical hydrodynamics in an expanding frame (Peebles, 1980):

$$\frac{\partial\delta}{\partial t} + \frac{1}{a}\boldsymbol{\nabla}\cdot[(1+\delta)\mathbf{v}] = 0 \tag{3.5}$$

[8] Formally, these equations are identical to the characteristic equations which represent the Vlasov equation. The characteristic curves are the curves in phase-space along which f remains constant. However, in this approach, a finite subset of the infinite characteristic lines is followed (Borgani and Kravtsov, 2011). In any case, Newtonian equations are used as, at the scales resolved by cosmological simulations, densities, velocities and distances are sufficiently small for Newtonian physics to be an excellent approximation (Peebles, 1993).

[9] In this text, we take the notation of Landau and Lifshitz (1987). Note, however, that other authors take different notations for the Eulerian and the Lagrangian (here, $\frac{\mathrm{d}}{\mathrm{d}t} \equiv \frac{\partial}{\partial t} + (\mathbf{u}\cdot\boldsymbol{\nabla})$) derivatives.

$$\frac{\partial \mathbf{v}}{\partial t} + \frac{1}{a}(\mathbf{v}\cdot\nabla)\,\mathbf{v} + H\mathbf{v} = -\frac{1}{a}\boldsymbol{\nabla}\phi - \frac{1}{\rho a}\boldsymbol{\nabla}p \tag{3.6}$$

$$\frac{\partial E}{\partial t} + \frac{1}{a}\boldsymbol{\nabla}\cdot[(E+p)\mathbf{v}] = -3H(E+p) - H\rho v^2 - \frac{\rho\mathbf{v}}{a}\boldsymbol{\nabla}\phi \tag{3.7}$$

where ρ is the gas density, $\delta \equiv \frac{\rho-\rho_B}{\rho_B}$ is the gas density contrast or gas overdensity, p is the pressure and $E \equiv \rho\varepsilon + \frac{1}{2}\rho v^2$ is the so-called *total* energy density, defined as the sum of the internal energy density ($\rho\varepsilon$; ε being the specific internal energy) and the comoving kinetic energy density.

Once the background cosmology is solved, and provided that ϕ (coupled to the rest of components through Eq. 3.4) is known, the system (3.5)–(3.7) has 5 equations and 6 unknowns (namely, δ, $\mathbf{v}$, E and p). An equation of state, $p = p(\rho, E)$, is required to close the system. The most common choice is the equation of state of an ideal gas,

$$p = (\gamma - 1)\rho\varepsilon, \tag{3.8}$$

where γ is the adiabatic exponent.

At first glance, Eqs. (3.5)–(3.7) look slightly similar to the regular, classical equations of fluid dynamics (cf. Landau and Lifshitz, 1987, §1, 2 and 6). Despite the increased complexity with respect to their classical analogs, they retain the same meaning: mass conservation (Eq. 3.5), momentum conservation (Eq. 3.6) and energy conservation (Eq. 3.7). However, they are expressed in terms of excess or *peculiar* quantities (density contrast, peculiar velocity, etc.) in the comoving frame.

Formally, the system comprising the 5 hydrodynamic equations can be written as a hyperbolic system of conservation laws (Quilis, Ibáñez, and Sáez, 1996), what makes it particularly suitable for its numerical resolution, as it shall be discussed in Sec. 3.2.

3.1.3 Making simulations more realistic: beyond gravity

Up to this point, only purely gravitational and hydrodynamical processes have been taken into account in the description of the evolution of cosmic inhomogeneities. These *non-radiative* models have provided important insight into structure formation (see Bertschinger, 1998 for a classical review), but do not suffice to fully explain galaxy formation (star formation, metal enrichment, etc.) and to correctly describe the thermodynamical properties of the ICM (e.g., the breaking of self-similarity in the inner regions of clusters). Therefore, some non-gravitational processes should be responsible for accounting for these effects. Typically, they are phenomenologically parameterised and included as source terms in the energy equation (Eq. 3.7). Including realistic baryonic feedback in cosmological simulations is a vibrant topic of ongoing research. Here, we shall only briefly mention the basic processes that are usually accounted for in simulations, while more in-depth reviews cover this topic extensively (Borgani and Kravtsov, 2011; Planelles, Schleicher, and Bykov, 2015)

For stellar formation, as these processes occur at scales several orders of magnitude below the distances resolved by cosmological simulations, phenomenological prescriptions capable of describing the overall observed star formation properties are implemented. Stars are usually included as an additional particle species. However, it is worth noting that these particles are much more massive than individual stars

and represent whole single-age stellar populations with average quantities. A first important byproduct of stellar evolution is the production of metals[10], which eventually get spread by the cosmic flows and chemically enrich the ICM (Borgani and Kravtsov, 2011).

In order to explain the breaking of self-similarity in clusters' inner regions, a combination of cooling and heating mechanisms is usually adopted. The main source of cooling is radiative cooling. However, including only this process leads to several undesirable results, amongst which overcooling (which produces excessive star formation rates) and an increased central ICM temperature could be mentioned. To overcome these problems, some sources of heating need to be accounted for. Linked to star formation, stellar feedback via SNe injects energy that could, in principle, offset overcooling and reduce the stellar mass fractions. However, this mechanism by itself is not efficient enough. The preferential heating mechanism, as of today, is AGN feedback, resulting from the accretion of matter onto supermassive black holes. In any case, building these effects in simulations is still a matter of ongoing research and important uncertainties remain present (Planelles, Schleicher, and Bykov, 2015).

3.1.4 Initial conditions

The previous sections cover how density perturbations evolve with cosmological time. However, in order to solve the problem, an initial condition has to be given.

Inflation predicts that the primordial density fluctuations are a particular realisation of a Gaussian Random Field (Peebles, 1993), which is statistically fully described by its primordial power spectrum, $P(k) \equiv \langle|\delta(\mathbf{k})|^2\rangle = A_s k^{n_s}$, where $\delta(\mathbf{k})$ is the Fourier transform of $\delta(\mathbf{x})$. In the linear theory of structure formation (applicable while $|\delta(\mathbf{x})| \ll 1$, i.e., at very high redshifts), a transfer function, $T(k)$, gives the evolution of the power spectrum. Thus, the shape of the power spectrum after recombination ($z \simeq 1000$) can be determined and written as $P(k) = A_s|T(k)|^2 k^{n_s}$. The details about the transfer function will not be covered here, but can be found in Theuns (2016), for instance.

From this point, initial perturbations can be got at $z \simeq 1000$ and evolved in time using analytical or semi-analytical (e.g., the Zel'dovich approximation; Peebles, 1993) methods up to a more recent redshift, $z \simeq 50 - 100$. This sets the initial conditions for the numerical simulation.

3.2 Numerical techniques implemented in cosmological simulations

In Sec. 3.1, the basic skeleton of the mathematics behind structure formation has been presented:

- $6N$ first-order in time, coupled ODEs, i.e., Eqs. (3.2) and (3.3) for each of the N particles, in order to solve the dynamics of the collisionless component (DM).
- A hyperbolic system of 5 coupled, highly non-linear PDEs, Eqs. (3.5)−(3.7). The equations are first-order in temporal and spatial derivatives of the variables.

[10] Heavy elements.

It can be shown that the system can be rewritten in conservation form, i.e.

$$\frac{\partial \mathbf{u}}{\partial t} + \frac{\partial \mathbf{f}(\mathbf{u})}{\partial x} + \frac{\partial \mathbf{g}(\mathbf{u})}{\partial y} + \frac{\partial \mathbf{h}(\mathbf{u})}{\partial z} = \mathbf{s}(\mathbf{u}) \tag{3.9}$$

where $\mathbf{u}$ is the vector of *unknowns*, $\mathbf{u} \equiv (\delta, (1+\delta)v_x, (1+\delta)v_y, (1+\delta)v_z, E)$; $\mathbf{f}$, $\mathbf{g}$ and $\mathbf{h}$ are the fluxes; and $\mathbf{s}$ is the source term vector. See Quilis, Ibáñez, and Sáez (1996) for the explicit expression of these fluxes and sources.

- An elliptic PDE, i.e. Poisson's equation (3.4), which couples both previous components. This equation is second order in the spatial derivatives of the peculiar potential.

Naturally, additional physics (as discussed in Sec. 3.1.3) could introduce new species (e.g., stellar particles, metals, etc.; which would require additional equations) or new sources due to feedback phenomena (which would imply adding new source terms in $\mathbf{s}(\mathbf{u})$).

Through the next pages, we shall present the main families of numerical techniques used to tackle each of the points listed above.

3.2.1 Basic concepts

Numerical techniques for the resolution of these equations can be split into two broad families, according to the element which is discretised in the description of the numerical method (Dolag et al., 2008):

- *Grid-based* simulations: the computational domain is split in a finite number of cells (volume discretisation). Each of the volume elements ought to be small enough to provide the desired resolution, but must still be thermodynamically macroscopic for the physical description in Sec. 3.1 to be valid.

- *Particle-based* simulations: discretisation is performed on a mass basis. In order to recover a continuous field description, a smoothening method is required.

As it will be seen through the following sections, in a real cosmological simulation both approaches can coexist in the same code, i.e., different components can receive different numerical treatments.

3.2.2 Evolving the dark component

Once the peculiar potential, ϕ, has been solved (see Sec. 3.2.4 for details) and the global gravitational field ($\boldsymbol{\nabla}\phi$) is known, Eqs. (3.2) and (3.3) are just a set of $6N$ first-order ODEs, coupled in pairs (x^i_α and v^i_α, for components $i = 1, 2, 3$ and particles $\alpha = 1, ..., N$). For simplicity, let us focus on one of these two-equations subsystems. The equations can be addressed using regular numerical ODE solvers.

These algorithms can be split into two main groups: explicit and implicit methods. The former ones only use information about previous time steps in order to find the state of the system at a later time. Conversely, the latter techniques use previous and next time steps in order to do so. As a trivial example, the time step rule for an equation $\dot{\mathbf{y}} = \mathbf{f}(\mathbf{y})$ in an explicit and an implicit Euler method would be, respectively:

$$\mathbf{y}_{n+1} = \mathbf{y}_n + \mathbf{f}(\mathbf{y}_n)\Delta t \tag{3.10}$$

$$\mathbf{y}_{n+1} = \mathbf{y}_n + \mathbf{f}(\mathbf{y}_{n+1})\Delta t \tag{3.11}$$

In principle, implicit techniques can offer smaller numerical error but, as $\mathbf{y}_{n+1}$ appears on the right-hand side of Eq. (3.11), they would in general require iteratively solving for $\mathbf{y}_{n+1}$, thus increasing the computational cost. Consequently, N-Body simulations most usually lean towards explicit implementations (Dolag et al., 2008).

The main limitation of explicit methods is the fact that the derivative is assumed to be constant over the integration interval Δt. A broad variety of methods for higher-order ODE integration exist, many of which are just particular realisations of Runge-Kutta methods. These techniques use Newton-Cotes formulae to the desired order to compute the integral $\int_t^{t+\Delta t} \mathbf{f}(\mathbf{y}(t), t)\mathrm{d}t$ using several intermediate points. Other solutions for this particular problem are found by means of more sophisticated algorithms (e.g., the leap-frog method, in which velocities and positions are shifted by half a time step, so that velocities are always computed in the centre of the interval used for evolving positions and vice-versa), which provide an increase in accuracy without the need to decrease the timestep. Bertschinger (1998) and Dolag et al. (2008) compile more complete reviews of the numerical methods for this problem.

The most computationally expensive part in N-Body simulations is solving the gravitational force, which will be reviewed in Sec. 3.2.4. In some methods, a continuous, grid description needs to be recovered from the particle distribution. In these cases, smoothening methods are used in order to assign particles to cells. The basic idea is assigning a kernel $W(\mathbf{x}_i - \mathbf{x}_m)$ to each particle, so that the density of cell m can be written as

$$\rho_m = \frac{1}{h^3} \sum_i m_i W(\mathbf{x}_i - \mathbf{x}_m), \tag{3.12}$$

where the index i runs over all the particles and h is the cell side length. There are many schemes, amongst which we could cite Nearest Grid Cell (NGC), Cloud-in-Cell (CIC) and Triangular-Shaped Cloud (TSC), in increasing order of complexity (sharing the particles' mass amongst the nearest 1, 8 and 27 cells), respectively.

3.2.3 Evolving the gas component

Hydrodynamical techniques are usually divided into two blocks, parallel to the two specifications of the flow field: Lagrangian and Eulerian techniques (Dolag et al., 2008).

Lagrangian schemes. Even though grid-based Lagrangian methods do exist (see below, *Moving mesh schemes*), most of them are particle-based. By abuse of terminology, "Lagrangian" and "particle-based" are very often used interchangeably. We shall restrict this description to gridless, particle-based codes. The most extended implementations are the Smoothed-Particle Hydrodynamics (SPH) techniques (Borgani and Kravtsov, 2011).

In these techniques, fluid elements are represented by particles, which obey some dynamical equations based on the Lagrangian form of Eqs. (3.5)−(3.7). The absence of any grid constraining the spatial resolution naturally confers these methods an adaptive character (in the sense of a huge dynamical range) at a reduced computational cost. However, SPH has some severe limitations. First, these methods have limited ability to properly describe shocks and strong gradients (although it can be partially overcome with the use of artificial viscosity; Dolag et al., 2008). Also, low-density regions (like the cosmic voids) do not get properly described.

Eulerian schemes. The most widely used implementations are the ones using grid-based High-Resolution Shock-Capturing (HRSC) techniques (Quilis, Ibáñez, and Sáez, 1994). Physical quantities are assigned to cells' centres. At each time step, the fluxes must be computed. In order to accurately describe discontinuities, these quantities are reconstructed to compute the fluxes at cells' boundaries (a thorough description of the possible implementations is described in Dolag et al., 2008). The main advantage of these methods is that they can correctly resolve shocks and discontinuities within a few cells, thus overcoming one of the main limitations of SPH. With the equations written in conservation form, Eq. (3.9), particularly suitable techniques are the ones based on Riemann solvers, as they grant the total conservation of the physical quantities (mass, momenta and energy). However, the Eulerian nature of the codes, i.e., working on a fixed grid, constrains the spatial resolution and increases the computational cost when the scenario requires higher resolutions.

The situation has reversed in the last 20 years, due to the adoption of AMR schemes in cosmological simulations. AMR allows to gain resolution (both in space and time) in certain regions of interest (e.g., high-density, steep gradients, etc.). Thus, if only a small fraction of the total volume needs to be refined (as is often the case in cosmology), a significant enhancement in resolution can be achieved without a dramatic increase in computational cost, what makes HRSC methods technically competitive with SPH (Borgani and Kravtsov, 2011).

Moving mesh schemes. These schemes are inherently Lagrangian, but grid-based. By following the fluid motion, the –initially uniform– grid gets distorted. Moving mesh –or *hybrid*– methods bring together the advantages of Eulerian and Lagrangian schemes. They can provide high spatial resolution as well as an accurate description of shocks.

As a final remark, it is important noting that, even though all these techniques aim to solve the same equations, their discretised versions are not necessarily equivalent. Therefore, systematic differences between different families of codes can arise (Borgani and Kravtsov, 2011).

3.2.4 Solving for the gravitational force

Gravity couples the different material components in the evolution of cosmic inhomogeneities and, accordingly, the algorithms to compute such gravitational force are one of the key ingredients of cosmological simulations.

The most straightforward idea in a particle-based simulation would be directly computing the force (or the potential) by summing the contributions of all the parti-

cles present in the computational domain. However, this approach is computationally unfeasible for large simulations, as the required time for such calculation scales as $\mathcal{O}(N^2)$, being N the number of particles. Several alternatives to this *direct summation* procedure exist. Here, a brief overview of the main techniques is presented, while complete reviews on the topic can be found in the bibliography (e.g., Dolag et al., 2008).

The particle-mesh (PM) method reduces the computation time by computing the forces on a grid. As described in Sec. 3.2.2, particles are assigned to the grid using some of the interpolation methods mentioned above. From the total density defined on the grid, Poisson's equation (Eq. 3.4) is solved, either in configuration space (by performing finite differences) or in Fourier space (by using Fast Fourier Transforms (FFTs)). Then, $\boldsymbol{\nabla}\phi$ is computed by finite-differencing the potential and interpolated back to particles. This algorithm reduces substantially the computational demand, down to $\mathcal{O}(N \log N)$. However, in the presence of strong overdensities, the force resolution gets importantly damaged due to having assigned particles to grid points.

The particle-particle/particle-mesh (P^3M) method overcomes this limitation by splitting the potential into two contributions: a short-range one, which is computed by direct summation; and a long-range one, for which the PM scheme is used.

Another family of algorithms to numerically solve Poisson's equation are the gridless *tree methods*. The basic idea behind these algorithms is grouping distant particles together into a large "macroparticle", which is accounted for using multipolar expansions.

4 | Simulation and Analysis Tools

All the analyses described in this work have been performed upon a simulation carried on with the cosmological code MASCLET. Its main features are explained in Sec. 4.1. The problem of structure finding in full-cosmological simulations is introduced in Sec. 4.2, where the halo finder ASOHF, which is used in this work, is presented. Finally, Sec. 4.3 covers the details of the simulation analysed in this text.

4.1 Cosmological simulations with MASCLET

The cosmological code MASCLET (Mesh Adaptive Scheme for CosmologicaL structurE evoluTion; Quilis, 2004) is an Eulerian hydrodynamical coupled to N-Body code primarily designed for cosmological applications. Below, we review its main features.

The AMR strategy. One of the main features of MASCLET is the AMR scheme, which provides an increased resolution wherever it is required (in practical terms, the refinement criteria can be varied depending on the application). The code handles several levels of refinement, so that the resulting mesh structure consists on a hierarchy of nested patches.

The hierarchy is recomputed every global time step. This procedure comprises several tasks. First, *refinable* cells at level ℓ are identified and patches are generated and grown around them according to some criteria until all refinable cells are covered by patches. Second, patches are remapped with a finer grid at level $\ell+1$. In MASCLET, the resolution increase between consecutive levels is $\frac{\Delta x_\ell}{\Delta x_{\ell+1}} = 2$. Last, the quantities on the finer grid (only for the newly refined cells) are reconstructed from the coarser grid by trilinear interpolation.

This process is repeated for all the refinable levels ($\ell = 0, \ldots, n_\ell - 1$, where n_ℓ is the number of refinement levels). See §5.3 in Planelles (2011) for a more detailed summary of this process. Note that overlaps between the different patches, i.e., cells at the same position belonging to different patches, can be produced by this process.

The hydro solver. The hydro solver is based on HRSC techniques, briefly treated in Sec. 3.2.3 (see Quilis, Ibáñez, and Sáez, 1994 and Quilis, Ibáñez, and Sáez, 1996 for more details on this particular implementation), which exploit the fact that the system can be written in conservation form (Eq. 3.9). Amongst its most basic features, it uses parabolic reconstruction in order to compute the values of the quantities, $\mathbf{u}$, at the interfaces from the cell-averaged quantities. From these values, the Riemann solver computes the fluxes. Once the fluxes at each interface are known, advancing in time only requieres solving ODEs, which, in this implementation, is done with a third-order Runge-Kutta method (see Sec. 3.2.2).

Advancing DM particles in time. DM particles are evolved in time according to Eqs. (3.2) and (3.3) using a second-order Lax-Wendroff scheme, which uses an intermediate step $t^{n+\frac{1}{2}} = t^n + \frac{\Delta t}{2}$ as follows:

1. The intermediate step, $n+\frac{1}{2}$, is computed:

$$\mathbf{x}^{n+\frac{1}{2}} = \mathbf{x}^n + \frac{1}{2}\frac{\mathbf{v}^n}{a^n}\Delta t \tag{4.1}$$

$$\mathbf{v}^{n+\frac{1}{2}} = \mathbf{v}^n - \frac{1}{2}\left[\frac{\boldsymbol{\nabla}\phi^n}{a^n} + H^n\mathbf{v}^n\right]\Delta t \tag{4.2}$$

2. Then, step $n+1$ is reached by:

$$\mathbf{x}^{n+1} = \mathbf{x}^n + \frac{\mathbf{v}^{n+\frac{1}{2}}}{a^{n+\frac{1}{2}}}\Delta t \tag{4.3}$$

$$\mathbf{v}^{n+1} = \mathbf{v}^n - \left[\frac{\boldsymbol{\nabla}\phi^{n+\frac{1}{2}}}{a^{n+\frac{1}{2}}} + H^{n+\frac{1}{2}}\mathbf{v}^{n+\frac{1}{2}}\right]\Delta t \tag{4.4}$$

The potential at $t^{n+\frac{1}{2}}$, $\phi^{n+\frac{1}{2}}$, is computed by linear extrapolation from ϕ^{n-1} and ϕ^n. Finally, after each position update, the code uses a TSC scheme to recover the grid description for the DM density. Note that, because of the nested hierarchy of the grid, the same particle can contribute to several patches at different levels of refinement (with different cloud sizes, depending on the level).

Gravity solver. The gravitational force is computed from the total density field using a PM implementation which benefits of the AMR structure of the grid. For the coarse grid ($\ell = 0$), the gravitational potential is found by computing the FFT of the total overdensity field, $\delta_T(\mathbf{k})$, and solving Poisson's equation in Fourier space, where it reduces to a product with the Green's function (which ought to be computed each time the grid is rebuilt). Another FFT yields the potential in configuration space.

For the refinement levels ($\ell > 0$), the potential has to be solved taking into account the boundary conditions imposed by the parent grid. Although a complete discussion falls beyond the scope of this work, `MASCLET` addresses this problem using a *successive overrelaxation method*, which solves for the potential iteratively. A more detailed specification of these procedures can be accessed in Dolag et al. (2008).

Other elements. The code includes a battery of additional physics, besides gravity and hydrodynamics. Because of space limitations, we only mention them without entering into too much depth. More details can be found in Quilis (2004); Planelles (2011); Quilis, Martí, and Planelles (2020), following the historical development of the code. A phenomenological parametrisation of stellar formation, which includes feedback from SNe, is incorporated. Stars produce metals, which get advected with the gas. Several cooling and heating mechanisms are included in the energy equation (Eq. 3.7). AGN feedback is also implemented.

Recently, a new version of the code which includes the description of a cosmological magnetic field has been presented (Quilis, Martí, and Planelles, 2020).

4.2 Structure identification

A crucial step in our analyses has been the identification of galaxy clusters. As DM is the dominant material component and it leads the collapse of clusters (see Sec. 2.2.3), the most common way to look for clusters focuses on identifying their underlying DM haloes (e.g. Planelles and Quilis, 2009).

4.2.1 The problem of halo finding

Simulations generate enormous amounts of raw information, which has to be processed and interpreted in order to make their results directly comparable to observations. In this respect, faithfully finding and describing DM haloes in a N-Body simulation is a fundamental, yet not completely closed issue (Knebe et al., 2011). The basic idea behind halo finders, when applied to N-Body simulations, is to identify gravitationally bound groups of DM particles and, potentially, their substructure and assembly history.

There are two fundamentally different approaches to the problem, which are briefly discussed below:

Friends of Friends (FoF). These were the first algorithms to emerge (Davis et al., 1985). The basic idea consists in grouping DM particles which are closer than some *linking length* together. This linking length is usually set to some fraction of the mean particle separation in the whole simulation domain. The resulting collection of neighbours of neighbours is considered a halo, whose mass can be estimated by simply adding up the masses of all the constituent particles. Amongst the main drawbacks of these implementations are the need to –manually– specify a linking length and the possibility for nearby haloes to get spuriously linked through the so-called *linking bridges*.

Spherical Overdensity (SO). The basic implementation of this method (Lacey and Cole, 1994) consideres the mean overdensity in spherical regions as the criterion to detect haloes, and compares it to the virial overdensity given by the top-hat collapse model (Eq. 2.6). The main weakness of this scheme is the fact that it enforces spherical symmetry on the objects, while real haloes are more often triaxial or even irregular (see Sec. 2.2.1). Nevertheless, this algorithm has the important advantage of not requiring to fix a linking length.

During the late 1990s and the 2000s, a flourishing amount of new algorithms arose, further extending the ideas of one or both of the previously reviewed. Although we may not cover them in this text, Knebe et al. (2011) shows the results of a comparison project amongst a number of halo finders.

4.2.2 The halo finder `ASOHF`

`ASOHF` (Adaptive Spherical Overdensity Halo Finder; Planelles and Quilis, 2010) is a SO halo finder especially designed to take advantage of the AMR structure of `MASCLET` (although a standalone version, which can be coupled to the outputs of a general N-Body simulation, also exists).

The basic procedure relies on the idea of the previously explained SO method, but the particular implementation includes several additional steps aimed to improve the performance and avoid some of the possible limitations.

First, the code identifies the density maxima using the density field computed over the AMR hierarchy of grids. For each maximum, its corresponding virial radius is found as the radius which encloses a density $\Delta_{\rm vir,c}(z)\rho_c(z)$. This gives a rough approximation of haloes' positions, masses and radii. Then, the overlaps amongst haloes are considered. Pairs of haloes sharing more than 40% of the minimum of their masses are joined together and the new position, radius and mass is computed. This provides a tentative list of haloes.

From this point on, the code works solely on the DM particle distribution, instead of the smoothed density field. As particles are not limited by cells boundaries, a more precise estimation of the physical quantities of the halo is, thus, achieved. Further checks that are finally performed include:

(i) Whether the particles are gravitationally bound. In order to do so, particle velocities are compared to their local escape velocity. Unbound particles are pruned and do not contribute to the halo.

(ii) Whether the radially-averaged density profile is consistent with a NFW profile (Eq. 2.7).

The final output of the halo finder consists on a list of the haloes, with a precise estimation of the physical parameters of each (position, velocity, virial radius, moments of inertia, etc.).

This code is especially designed to identify a whole hierarchy of substructures (haloes within haloes). `ASOHF` accomplishes this by taking advantage of the AMR structure of `MASCLET` outputs and being able to perform the process of halo finding at each level of refinement independently. The results at each level are finally brought together by imposing several conditions to prevent misidentifications of subhaloes (see Planelles and Quilis, 2010 for more details).

Another distinctive feature of `ASOHF`, which is exploited in this work, is its ability to track the evolutionary history of DM haloes by building the merger tree (MT). DM particles in `MASCLET` are assigned a unique identifier. `ASOHF` takes advantage of this in order to find the shared mass between haloes at different code outputs, thus being able to compute a list of the *progenitor* haloes of a given structure.

4.3 Simulation details

The simulation we analyse in this manuscript has been performed with the cosmological code `MASCLET`, described in Sec. 4.1. The background model assumes flat ΛCDM cosmology with density parameters $\Omega_\Lambda = 0.69$, $\Omega_m = 0.31$ and $\Omega_b = 0.048$. The Hubble constant is set to $h = 0.678$, and the initial density fluctuations are generated using a spectral index $n_s = 0.96$ and an amplitude given by[11] $\sigma_8 = 0.82$.

The simulation domain is a cubic region of comoving side length 40 Mpc, which is discretised at the base level ($\ell = 0$) with 128^3 cells. This yields a coarse resolution

[11] σ_8 is the rms amplitude of the linear perturbations on a cubic window of side $8\,h^{-1}$ Mpc. Giving σ_8 is equivalent to giving A_s, as both quantify the amplitude of the primordial density fluctuations.

of $\sim 310\,\mathrm{kpc}$. Following the AMR strategy, up to $n_\ell = 9$ levels of refinement are allowed, giving a peak resolution of $\sim 610\,\mathrm{pc}$.

The initial conditions are set at $z = 100$, using a constrained realisation in order to generate a massive cluster in the centre of the domain by $z \simeq 0$ (see Quilis, Planelles, and Ricciardelli, 2017; Planelles et al., 2018 for more details about the initial conditions in this simulation).

The refinement criteria is based on the local baryonic and DM density. A low-resolution run is first performed until $z = 0$ in order to pick the regions to be initially refined, up to level $\ell = 3$. Four species of DM particles are used. Initially, the coarse grid is sampled with the most massive particles, while the subsequent levels of refinement are sampled with particles 8, 64 and 512 times lighter mass. With these particles, the best mass resolution is $\sim 2 \times 10^6 M_\odot$, which would be the equivalent of filling the simulation volume with 1024^3 particles.

The simulation includes several cooling and heating mechanisms, star formation, metal enrichment, feedback from type-II SNe, etc. (as described in Sec. 4.1). However, feedback from stellar winds, type-Ia SNe and AGN are not included in this run.

5 | Results and Discussion

As motivated in Sec. 2.2, accretion plays an important role in shaping the dynamical and thermodynamical properties of gas in clusters. In the recent years, several studies have been aimed to characterise the statistical effects of accretion using big samples of clusters (e.g. More, Diemer, and Kravtsov, 2015; Y. Chen et al., 2020), putting emphasis on the effects on the scaling relations (Lau et al., 2014; H. Chen et al., 2019). Instead, in this work we try to analyse in further detail the physics of accretion on a small sample of clusters, presented in Sec. 5.1. The subsequent sections cover different analyses performed on this sample, encompassing the determination of accretion rates and the exploration of their relation to clusters' environments, as well as the inner structure of clusters and the angular distribution of mass accretion flows.

5.1 Selection of objects

From the simulation described in Sec. 4.3, we have identified 8 DM haloes with virial mass $M_{\rm vir} > 10^{13} M_\odot$ at $z = 0$. These objects (labelled CL01 to CL08) constitute the preliminary sample to be studied, and their most basic properties are listed in Table 2.

Two of these objects have total masses above $10^{14} M_\odot$ at $z = 0$ and can be fully considered galaxy clusters. The remaining six objects have masses below $10^{14} M_\odot$, corresponding to low-mass clusters or groups. This qualitative distinction is of utmost importance for the interpretation of our results: while more massive objects gravitationally dominate their surroundings, one does not expect the same to happen for the smaller objects. Low-mass clusters and groups are still subject to strong gravitational influence from nearby larger objects, which could produce a wide variety of effects: tidal interactions, gas stripping, etc. (Tormen, Moscardini, and Yoshida, 2004; Cen, Pop, and Bahcall, 2014; Quilis, Planelles, and Ricciardelli, 2017)

The `MASCLET` refinement strategy does not allow to refine $\ell = 0$ cells in the boundary of the computational domain. Hence, matter close to the boundary has been tracked with low spatial and force resolutions, and the dynamics in this region are not reproduced as faithfully as in the rest of the simulation box. Due to this instrumental limitation, cluster CL05 has been excluded from the sample.

5.1.1 Main branch of the merger tree

We are interested in following the evolution of properties of these clusters. In concordance with previous works (e.g. Planelles and Quilis, 2009; H. Chen et al., 2019), we define the MT of a cluster as the MT of its underlying DM halo. This procedure is well motivated by the idea of DM collapse leading the formation of structures depicted in Sec. 2.2.3.

Using `ASOHF`, given a halo at some iteration, we can extract a list of its *progenitor haloes* (i.e., the haloes at the previous code output which have particles in common with the given halo), and the fraction of progenitor's mass given to the descendant halo. We refer to these data as the *full merger tree* of a given DM halo. However,

TABLE 2: Sample of clusters studied in this work and its main properties at redshift $z = 0$. x, y and z refer to the DM center of mass comoving coordinates. The masses $M_{\rm DM}$ and $M_{\rm gas}$ are measured inside $R_{\rm vir}$. The last column specifies the clusters which have been excluded from later analyses.

cluster	x (Mpc)	y (Mpc)	z (Mpc)	$R_{\rm vir}$ (Mpc)	$M_{\rm DM}$ ($10^{13}M_\odot$)	$M_{\rm gas}$ ($10^{13}M_\odot$)	Excluded
CL01	0.1	0.0	0.1	1.99	42.9	4.56	
CL02	-3.2	4.9	-14.9	1.26	10.9	1.33	
CL03	17.0	-3.0	9.4	0.960	4.82	0.656	
CL04	10.7	-2.5	2.0	0.948	4.63	0.437	
CL05	19.5	-2.8	2.0	0.811	2.91	0.364	[a]
CL06	-14.6	-1.0	-11.0	0.707	1.92	0.224	
CL07	-10.4	1.1	10.8	0.658	1.55	0.144	[b]
CL08	-15.0	-4.6	1.9	0.609	1.23	0.117	

[a] This object is poorly described, due to the fact that it is close to the simulation domain's boundary.
[b] This object cannot be followed beyond $z \sim 1$, as it mass decreases strongly with increasing redshift.

in order to study continuous accretion, we have built the *reduced merger tree*, which only contains the main progenitor of each halo at a given iteration. There is not a unique definition, as different works opt for different approaches (e.g., check the references in the previous paragraph). We have tested three different strategies:

- The *backwards* strategy: amongst all the progenitor haloes, the main progenitor is picked as the one which contributes the most (the one which gives the most mass) to the descendant halo. This strategy is followed in, e.g., Tormen, Moscardini, and Yoshida (2004).

- The *forwards* strategy: the main progenitor is picked as the one which gives the largest fraction of its mass to the descendant halo.

- The *shared mass* strategy: the main progenitor is chosen as the one which the descendant halo shares the larger mass of *most-bound particles* with. In our particular implementation, we define the most-bound DM particles as the ones within a radial distance of $r_b = 0.5R_{2500m}$ from the halo barycenter.

In principle, these three methods do not necessarily yield the same results. Intuitively, the backwards strategy is a reasonable choice to study the evolution of a cluster sample focusing on the objects at $z = 0$. Likewise, the forwards strategy better captures the evolution of a cluster sample at some $z_{\rm in}$ towards the present time. Last, the shared mass strategy is physically motivated by the fact that cluster interiors remain less perturbed by the infall of substructures (More, Diemer, and Kravtsov, 2015), although it implies stronger assumptions on the sphericity and relaxedness of the objects.

For our cluster sample, these three methods only differ in the reduced merger tree of clusters CL02 and CL03, and these differences are restricted to only two and one snapshots, respectively, at high redshift ($z \simeq 1$) after which the evolutionary lines converge again. Careful examination of these situations reveals that the backwards

and forwards strategies tend to pick the higher mass parent; while the parent chosen by the shared mass strategy is normally a lower mass one which may have collided with the main cluster with a low impact parameter. The agreement amongst the three methods points out the robustness of the reconstructed reduced merger trees. For the rest of this project, we have chosen the evolutionary lines according to the backwards strategy.

Within these analyses, CL07 has only been followed up to $z \sim 1$. For earlier times, its mass decreases strongly and it is no longer found by `ASOHF`. Hence, it has been excluded from subsequent analyses.

5.1.2 Measurement of masses and radii

The previous analyses leave our sample with six objects to be studied, two of which (CL01 and CL02) can be regarded as massive clusters, and the rest being smaller clusters or groups.

With the aim of characterising the mass evolution of these clusters, we have measured the radii R_{200m}, $R_{\rm vir}$, R_{500m} and R_{2500m}, defined with respect to the DM particle distribution, by numerically solving Eq. (2.5), where the term $M_{\Delta_m} = \int_{r=0}^{r=R_{\Delta_m}} \rho_{\rm DM} {\rm d}^3 r$ can be computed as the sum of the masses of the particles inside a clustercentric radius R_{Δ_m}. This calculation has been performed for every code output from $z = 1.5$ to $z = 0$.

In order to boost convergence and minimize the number of required enclosed-mass computations, we use Brent's method (Brent, 1973), which combines secant and inverse quadratic interpolation methods and whose convergence is guaranteed for functions that change sign in some initial interval.

Once the different radii for each cluster at each iteration are known, the stellar, gas, DM and total masses have been obtained at each code output by integrating the densities over the corresponding spherical volumes.

5.2 Determination of mass assembly histories and mass accretion rates

5.2.1 Mass accretion history of the clusters in the sample

The evolution of the DM halo mass (according to one of its possible definitions) informs about its mass assembly history (MAH) (e.g., see Y. Chen et al., 2020, where this operative definition of the MAH is also used). The computations in the previous section provide the MAH of each of the components (stellar, gaseous and dark), for each of the clusters. In this section, we use these data in order to quantify the magnitude of the accretion phenomena onto each of the objects in the sample. Fig. 2 shows the MAH of the dark and the baryonic (gas and stars) components.

The left panel shows the evolution of the DM masses. As a general trend, all DM haloes display a mass growth, as a result of the accretion of surrounding matter and merger events. While some haloes grow at a relatively constant rate (e.g. CL08), others alternate sudden mass increases and more quiescent periods. This fact already points out at a division between merger events and smooth accretion, which is further explored in Sec. 5.3.

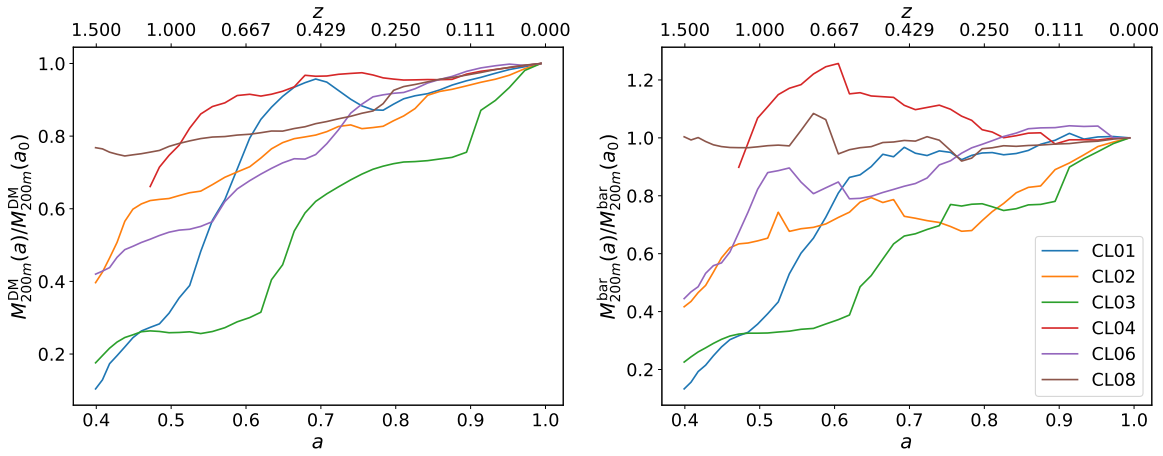

FIGURE 2: MAH of the selected clusters, for the DM component (left) and the baryonic component (right). Each curve has been normalised to the present-day mass of the corresponding component in each cluster.

The right panel presents the evolution of the baryonic masses. Baryonic mass has been chosen, instead of just the gas mass, as star formation activity can convert a significant amount of gas mass to stars at recent redshifts. Thus, measuring the evolution of gaseous masses does not only account for accreted mass, but is biased because of star formation. This effect is more intense in lower-mass systems, where star formation is more efficient (as mentioned in Sec. 2.2.1; see also Planelles et al., 2013). More massive systems do not exhibit significant differences between their DM and baryonic components, as far as mass evolution is concerned. The same is not true for the low-mass clusters and groups. Particularly salient is the case of CL04, whose baryon mass steadily decreases for $z \lesssim 0.7$. In the same direction, CL08 has a roughly constant baryonic mass with time, while its DM mass increases by more than 20% from $z = 1.5$ to $z = 0$. Less massive systems have shallower gravitational potential wells and their gas content is more likely to be unbound and lost due to dynamic (e.g., collisions with other systems, tidal interactions, etc.; Cen, Pop, and Bahcall, 2014; Quilis, Planelles, and Ricciardelli, 2017), hydrodynamic (e.g., shocks) and baryonic (e.g., heating due to SNe; Giodini et al., 2013) effects.

5.2.2 Mass accretion rate definitions

There are different ways of quantifying the strength of accretion onto clusters in the bibliography. Amongst them, we can count the following proxies for the mass accretion rate (MAR):

- The logarithmic slope of the enclosed mass (in a clustercentric sphere of radius R_Δ) with respect to the scale factor.

$$\Gamma(a) = \frac{\mathrm{d}\log M_\Delta}{\mathrm{d}\log a} \tag{5.1}$$

  This is the definition used in Adhikari, Dalal, and Chamberlain (2014), for example. However, a number of works substitute the derivative by a quotient

of differences over a wide time interval:

$$\Gamma_{[a_1,a_0]} = \frac{\log\left(M_\Delta(a_0)/M_\Delta(a_1)\right)}{\log\left(a_0/a_1\right)} \tag{5.2}$$

For example, Diemer and Kravtsov (2014) use $a_1 = 0.67$ ($z = 0.5$) and $a_0 = 1$; while H. Chen et al. (2019) find that Γ measured between $a_1 = 0.7$ and $a_0 = 1$ maximizes the correlations between the MAR and the ellipticity of the ICM. Note that these two definitions are related by $\Gamma_{[a_1,a_0]} = \frac{1}{\Delta \log a} \int_{\log a_1}^{\log a_0} \Gamma(a) \mathrm{d} \log a$.

- Lau et al. (2014) define their proxy for the instantaneous MAR as the quotient between the radially-averaged infall velocity of the DM particles measured at $r = R_\alpha$ and the circular velocity, $V_{\mathrm{circ},\Delta} = \sqrt{GM_\Delta/R_\Delta}$,

$$\alpha_\Delta = \frac{V_r^{DM}(r = R_\alpha)}{V_{\mathrm{circ},\Delta}}. \tag{5.3}$$

Note that more negative α_Δ implies more intense accretion.

These two definitions (Γ and α_Δ) are anticorrelated, although a large scatter exists (see Figure 5 in Lau et al., 2014). In this work, we have chosen to define the MAR as in Eq. (5.1). Furthermore, we define this quantity for each component (baryons and DM), which allows to study their different behaviour. We adopt the definition involving the derivative, which informs about the *instantaneous* accretion rate, rather than the average rate over a wide interval. The latter can better account for the global impact of accretion on the dynamical state (H. Chen et al., 2019), while the former better characterises the actual mass being accreted at a given time.

5.2.3 Determination of $\Gamma(a)$ for the clusters in the sample

Using the definition discussed above, we have computed the MAR for the clusters in our sample. In order to evaluate the numerical derivatives, we have tested two strategies aimed to minimise the contaminating effects of statistical noise:

- Computing the derivative using second-order central differences, and applying a gaussian filter to smooth the result.

- Directly computing the smoothed derivative using a Savitzky-Golay filter (Savitzky and Golay, 1964). These filters fit low-order polynomials using least squares methods, and then compute the derivative of the fitted polynomial. These methods have been long applied to noisy data in astrophysics (e.g., Press and Teukolsky, 1990).

Although the former is a more conventional approach, our tests show that gaussian smoothing fails to reproduce narrow peaks in the data, as they get excessively flattened. Savitzky-Golay filters, once their parameters are tuned, closely follow the data points while still preventing spurious peaks. In order to apply the Savitzky-Golay filter, the data points must be evenly spaced in $\log a$. In order to achieve this from initially unevenly spaced data, we have resampled the $M(a)$ curve by linear interpolation.

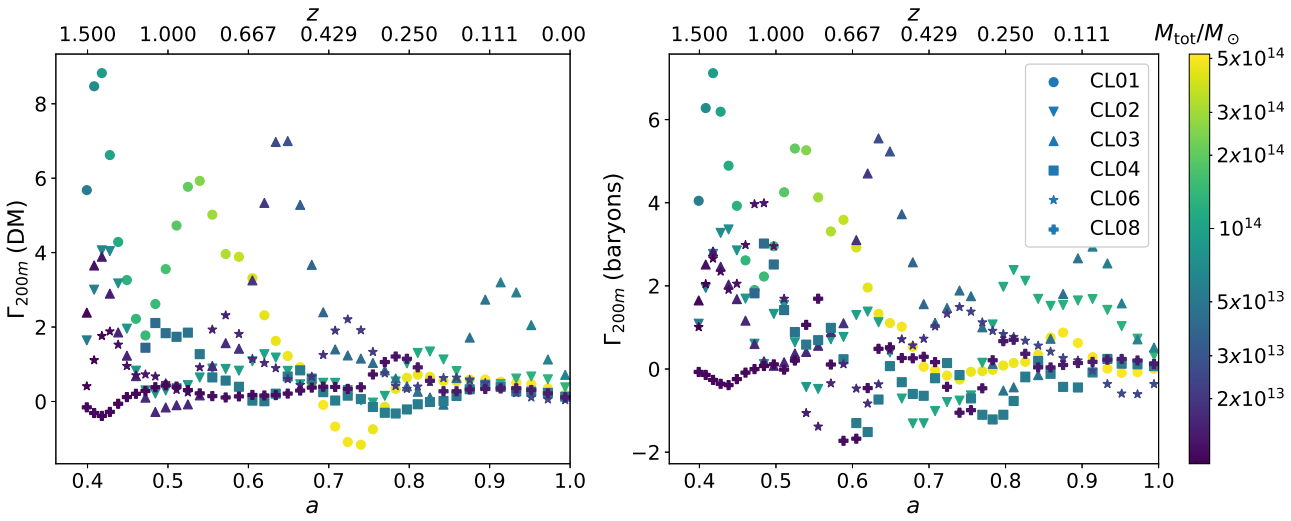

FIGURE 3: MARs of the selected clusters, for DM (left) and baryons (right). Colours encode the total mass (baryons + DM). The shape of the dots identifies each of the clusters according to the legend. Both, the colourbar and the legend, apply to both plots.

Using this technique, Fig. 3 shows the evolution of the MAR of the clusters in our sample, when measured for DM and for baryons.

The graphs show similar qualitative behaviour for the DM and baryon MARs, reflecting the fact that gas traces DM to a first approximation. However, the most prominent peaks (specially in the higher mass objects) are typically more pronounced for the dark component than their baryonic counterparts (e.g., compare the magnitude of Γ at the peak of accretion of CL01 at $z \sim 1.4$), implying that (i) there are systematic differences between DM and gas, and (ii) gas is generally accreting at a slower pace, when compared to DM. This trend has already been pointed out by other studies (see e.g. Lau et al., 2014, where a similar conclusion is drawn from studying the velocity profiles of both components). As opposed to collisionless DM, collisional gas is supported by pressure (which prevents a faster collapse), and experiences ram pressure from the ICM (Quilis, Planelles, and Ricciardelli, 2017), shocks, etc.

Fig. 3 displays a clear distinction between massive clusters (CL01, CL02 and, marginally, CL03) and low-mass clusters and groups (CL04, CL06 and CL08). Massive clusters often present strong peaks in their MAR curves, which indicate relatively short periods of intense accretion. These events are likely associated to major mergers, which are still frequent as clusters continue growing and collapsing by $z \sim 0$ (Walker et al., 2019). As can be seen from the colour scale, these events are the main contribution to the mass growth of clusters. We analyse in further depth the relation between mergers and accretion in Sec. 5.3.

Less massive clusters show flatter curves, pointing out that either they do not experience merger events as strong as their more massive homologues, or they undergo important mass losses during these events, as a consequence of their shallower potential wells. The latter idea is supported by the fact that the differences between baryonic and dark components are more remarkable in these systems. Clusters and groups with total mass $\lesssim 5 \times 10^{13} M_\odot$ do not seem to dominate as efficiently their neighbourhoods, and are therefore harassed by other systems.

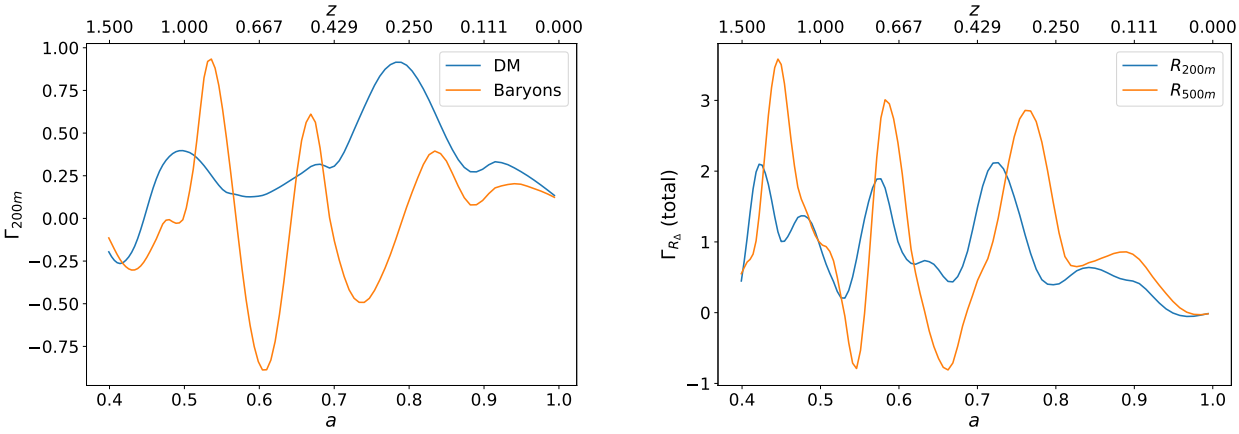

(A) CL08. Behaviour for different components

(B) CL06. Behaviour at different radii

FIGURE 4: Left panel compares the MAR for DM and for baryons, both measured inside R_{200m}. Right panel shows the total (baryons + DM) MAR measured inside R_{200m} and R_{500m}.

5.2.4 Dependence on radii and components

In order to better highlight the differences between the DM and baryonic MARs, Fig. 4a shows the corresponding curve for each component, for the particular case of the object CL08 (the lowest mass one). Dark matter shows a much smoother trend, while the gaseous counterpart exhibits important variability in its MAR. Furthermore, baryonic MAR peaks show a delay with respect to DM peaks. The redshift differences observed in the graph correspond to time differences in the order of $\sim 1\,\mathrm{Gyr}$. These results, again, hint that pressure support prevents faster accretion for the baryonic component.

Last, we have also analysed how do the MARs change with the reference radii. In that direction, Fig. 4b presents the total accretion rates (accounting for all gravitational matter) measured at R_{200m} and R_{500m}. The most remarkable feature of this graph is the delay between the Γ peaks at both radial marks. These delays, which are again in the order of $\sim 1\,\mathrm{Gyr}$, are present in all clusters displaying important peaks, and are consistent with the necessary time for infalling DM particles to cross the distance $R_{200m} - R_{500m}$.

5.3 Correlating accretion rates with mergers and surrounding density

As already pointed out in the previous section, the peaks in the MAR curves are most likely due to merger events. We define such mergers as events where two cluster-sized haloes (and their respective baryonic counterparts) encounter and share a significant amount of mass. In Sec. 5.3.1 we describe the procedure followed to identify and classify mergers. However, a significant part of the accreted mass can end up lying outside the R_Δ definition and, hence, the corresponding SO masses are not additive in merger events (Kravtsov and Borgani, 2012; More, Diemer, and Kravtsov, 2015). In Sec. 5.3.2, this fact is studied by determining the densities in the surroundings of the cluster and correlating them to the MAR.

5.3.1 Merger identification and classification

We have identified the mergers using `ASOHF` full MTs of DM haloes. Generally, and especially for massive haloes, `ASOHF` merger trees are able to identify many progenitor objects which contribute to a given halo in the following code output. However, most of them either contribute very little to the halo mass, correspond to low-mass substructures or are distant enough to be considered an artifact due to the spurious movement of a few particles. In order to identify halo mergers, we establish the following conditions:

I. The distance between the centers of mass of the two progenitor candidates is less than the sum of their virial radii, i.e., their spheres of radius $R_{\rm vir}$ intersect.

$$d_{ij} \leq R_i + R_j \tag{5.4}$$

This condition is conceptually similar to the one of H. Chen et al. (2019), who take a much inner radius, R_{500c}, to assess the merger times. In this work, we are not so interested in finding a particular merger time, but rather aim to describe the merging state of clusters. This motivates our choice of an outer radius.

II. Each of the progenitor haloes gives, at least, 1% of its (DM) mass to the descendant halo. Again, H. Chen et al. (2019) take a more stringent value (10%) which is consistent with their smaller interaction radii.

III. Each of the progenitor halo masses is larger than 1/10 of the descendant mass. Mergers with haloes of smaller mass are regarded as smooth accretion.

Following previous works (Planelles and Quilis, 2009; H. Chen et al., 2019), we define three accretion regimes, based on the maximum mass ratio between the progenitors:

- Major mergers: involve two haloes of comparable mass, and are relatively unfrequent. They typically have a large impact on the structure of haloes. We take a mass ratio of $1:3$ as the threshold for these events, in consistency with the previously cited works.

- Minor mergers: produce less significant disturbances on the objects, but are generally more frequent. Their mass lower threshold is more arbitrary. For example, H. Chen et al. (2019) take $1:6$, while Planelles and Quilis (2009) use $1:10$. In this work, we stick to the latter definition.

- Smooth accretion: systems which experience no mergers above the $1:10$ mass ratio threshold are considered to undergo smooth accretion.

In our sample, clusters CL01, CL02 and CL03 exhibit periods of major and minor merging activity. CL06 does not experience any major mergers, but only minor mergers. Last, no mergers have been identified in CL04 and CL08 and they are therefore smoothly accreting clusters throughout the considered interval $1.5 \geq z \geq 0$.

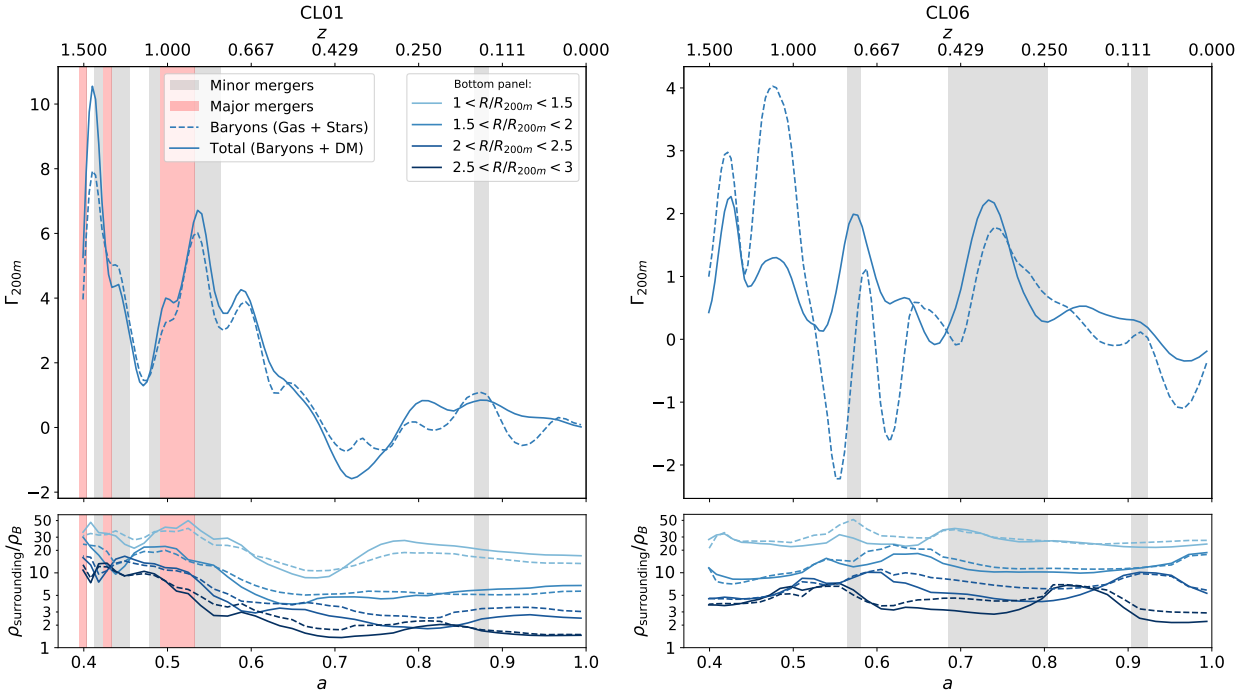

(A) CL01: major merger cluster

(B) CL06: minor merger cluster

FIGURE 5: Relation between the MAR, merger events and densities in the surroundings of the cluster, for two of the clusters. In each panel, the upper plot shows the MARs for the total mass (solid line) and baryonic mass (dashed line). The lower panel shows the surrounding density in various clustercentric radial bins, in terms of the background density of the Universe. The dashed line, corresponding to the baryonic density, has been normalized to the cosmic baryon fraction (i.e., has been multiplied by Ω_m/Ω_b). The legend in the left panel applies to both plots.

5.3.2 Surrounding densities

Motivated by the non-additiveness of SO masses in major mergers, we have quantified the densities in the surroundings of each cluster and its evolution with cosmic time in four non-overlapping, equally spaced radial bins, covering the region $1 \leq r/R_{200m} \leq 3$.

Fig. 5 exemplifies the results of these analyses for two clusters: CL01 (massive cluster which undergoes numerous major and minor mergers) and CL06 (low-mass cluster which only suffers minor mergers). Both panels show the total (solid lines) and baryonic (dashed lines) MARs, the merging regimes (background colour of the plot) and the surrounding densities (lower panels).

In the case of the massive CL01 cluster (Fig. 5a), as already pointed out in Sec. 5.2.3, differences in the MAR between different components (in this case, between the total mass, which is dominated by DM, and the baryonic one) are small in magnitude. In this case, peaks in the MAR are undoubtedly associated to (major) merger events, as it is the case of the displayed peaks at $z \sim 1.4$ and $z \sim 0.8$.

It is also interesting to note how high MARs are mantained for a long time after the merger has taken place (particularly salient is the case of the merger at $z \sim 0.8$). As already hinted in the introduction to this section, a significant part of the mass can be deposited beyond the R_{200m} boundary (More, Diemer, and Kravtsov, 2015). This

matter continues feeding the cluster –in a more quiescent way– for some time. In this respect, the lower panel shows how densities in the $1 \leq R/R_{200m} \leq 1.5$ region keep above $10\rho_B$ until $z \sim 0.5$; and even at regions as far as $2.5 \leq R/R_{200m} \leq 3$, densities are several times over the background value for a long time after the interaction.

Comparing the surrounding total and baryonic densities, the latter appears to evolve in a much smoother way than the former. At outer radii, $R \gtrsim 2R_{200m}$, baryon surrounding densities (when normalized to the cosmic baryon fraction) tend to be higher than total densities. This seems to reinforce the idea that gas, due to its pressure support, is deposited at larger radii than DM, which can more easily penetrate to inner regions. We find these general trends are shared for all the massive clusters in our sample which suffer major mergers.

The low-mass CL06 (Fig. 5b) exhibits significant differences in the behaviour of baryonic and total masses, as already found for CL08 in Sec. 5.2.4. The total MAR appears to experience peaks in correlation to the minor merger events. The gaseous component roughly follows these peaks, although their magnitude can differ significantly. There are also severe declines in the gas mass (negative Γ_{200m}), which reflect the inability of low-mass systems and groups to keep their gas inside R_{200m}. However, note that some of this $\Gamma_{200m}^{\text{baryons}} < 0$ may be associated, not to the gas being unbound and lost, but just deposited outside R_{200m} (e.g., see the important increase of surrounding baryon density when compared to total density at $z \sim 0.8$, while $\Gamma_{200m}^{\text{baryons}} < 0$). Part of this baryonic matter is reaccreted in the following peak at $z \sim 0.7$, while the rest might be expelled to larger radii, contributing to the increased baryon density at large radii at later times.

5.3.3 Temporal shift between surrounding densities and the MAR

For massive clusters, like CL01, the density in the immediate neighbourhood of the cluster shows remarkable resemblance with the MAR. However, a temporal shift between the surrounding density and the MAR is evident from the graphs. In order to quantify this shift, we compute the Spearman's rank correlation coefficient, r_s, of $\rho_{\text{surrounding}}(t)$ in the first radial bin with $\Gamma(t+\tau)$, and find the τ which maximises r_s. Spearman's coefficient assesses the monotonicity of the relation $\Gamma - \rho_{\text{surroundings}}$ without assuming linearity (as the Pearson's coefficient does). With this analysis, we draw the following conclusions:

- For the cluster CL01, when total masses are considered, an optimal shift of 900 Myr provides a rank correlation of $r_s = 0.803$. Restricting to the baryonic component enhances this correlation to $r_s = 0.895$, while increasing the time shift to 1.1 Gyr. Although these shifts can only be considered as rough estimates, we get consistent results, i.e. temporal shifts compatible with the crossing time for the faster infalling DM particles, and a higher shift for baryons. A similar trend is shown by cluster CL03, although in this case the correlations are weaker ($r_s = 0.744$ and $r_s = 0.691$, respectively).

- CL02, a massive cluster which only experiences a major merger at high redshift and experiences a more quiescent evolution therein (when compared to CL01 and CL03), shows weaker correlations, of $r_s = 0.623$ and $r_s = 0.572$.

- Less massive clusters do not display significant correlations between these variables, as a result of their limited ability to capture matter (especially, gas). Indeed, in the lower panel of Fig. 5b one sees a much flatter evolution of the surrounding densities.

5.4 Evolution of the density profiles

In Sec. 5.2 and 5.3, we have quantified accretion by studying the change in mass in a sphere enclosing most of the clusters' mass. In this section, we analyse how mergers and strong accretion impact the inner distribution of matter in clusters. In order to do so, we have computed the comoving density profiles of DM, gas and stars using $n_{\rm bins} = 100$ logarithmically spaced bins, from 100 kpc to 4 Mpc.

The central several hundreds of kpc in the radial profiles of density (or any other quantity) are considerably sensitive to the choice of center. There are many different choices: in simulations, amongst the most extended ones are the center of mass of the bound DM particles[12], DM or total mass density peaks, local gravitational potential minimum, etc. In Cui et al. (2016), the authors present a comparison of different choices of observable and how they influence the position of the center.

In order to compute the profiles, we have compared the non-recentered results with three recentering schemes: maximum of DM or total density and potential minimum. For the recentering runs, we have looked for the optimal cell inside a sphere of radius $0.5R_{2500m}$ around the center of mass of the DM halo. Our tests suggest that recentering to the potential minimum provides the overall most consistent results. The other options exhibit sudden displacements of the center (which can be attributed to the presence of substructures) and non-monotonically decreasing density profiles, which hint at miscentering issues. The choice of recentering to the potential minimum can be motivated by the fact that, by being the solution to the Poisson equation, the potential smoothes the spurious density peaks of the density field and better captures the overall distribution of matter in the cluster.

In Fig. 6, we represent the evolution of DM, gas and stellar radially-averaged comoving densities (top, middle and bottom rows, respectively) for clusters CL01, CL02 and CL06 (from left to right). On top of these plots, the green line indicates the virial radius. Note how the virial radii of CL02 (which only undergoes a major merger at $z \sim 1.4$) and CL06 (which only suffers minor mergers) are roughly constant, while CL01 (undergoing several major mergers) displays important variations in this magnitude.

Related to this, the inner regions of dark matter comoving density profiles are mostly constant in time for CL02 and CL06, suggesting that these structures are already collapsed by $z \sim 1$ and the innermost radii ($r \lesssim R_{2500m}$) do not get disturbed by minor mergers and smooth accretion. This result is consistent with More, Diemer, and Kravtsov (2015), who find that the mass inside $4r_s$ (being r_s the scale radius of the NFW profile, Eq. 2.7) evolves relatively slowly for $z \lesssim 1-2$. Conversely, CL01 does experience important disturbances in its DM profiles, especially around $z \sim 0.8$. The enhanced MAR during $1.1 \gtrsim z \gtrsim 0.7$ (see Fig. 5a) associated to the major merger event appears to substantially increase the central density.

[12] This corresponds to the center given by ASOHF.

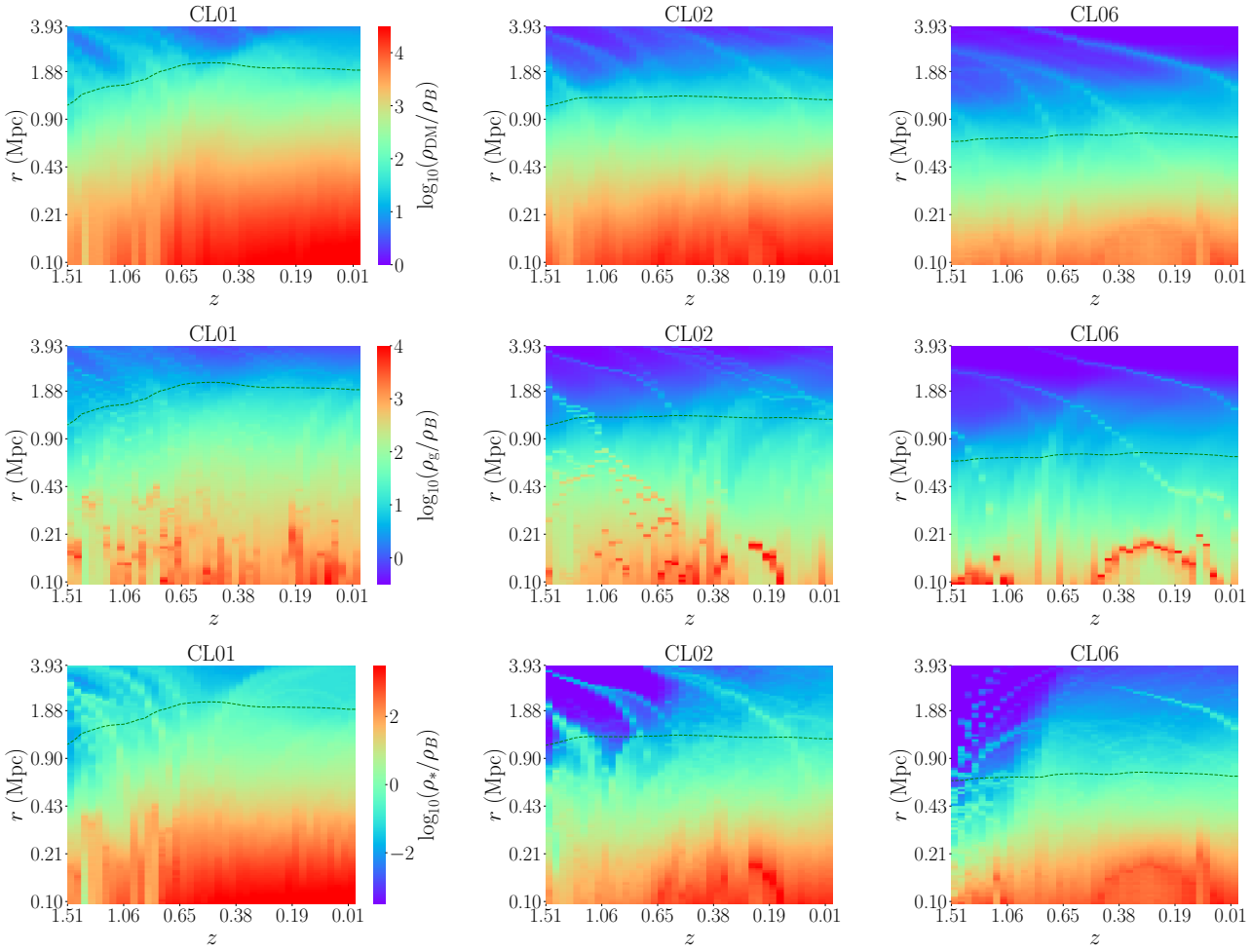

FIGURE 6: The panels show the evolution of the comoving density profiles of the different material components for three clusters, from $z \simeq 1.5$ to $z = 0$. Densities are always normalised to the background matter density of the Universe and the colour scale is logarithmic. Radial coordinates are comoving. From top to bottom, panels show DM, gas and stellar densities. From left to right, these quantities are presented for CL01, CL02 and CL06. The colour scale in the left plot of each row applies for all plots in the row. The green line in each panel indicates the virial radius.

Gas density profiles clearly show the presence of gas clumpiness, as well as miscentering (specially in the case of CL06). The centers of the gaseous and dark components do not necessarily coincide, especially when there is an important merging activity (i.e. departures from dynamical equilibrium). Stellar masses are mostly confined to the inner regions, with high densities only inside quite central radii ($\lesssim R_{500m}$), as only in these regions gas is dense enough and can cool efficiently to form stars.

Lines of decreasing radii with decreasing redshift indicate the presence of massive structures being accreted, mainly galaxy cluster mergers. These streams of matter are better recognised in the stellar component, as the stellar mass is more concentrated towards the center of the infalling cluster and leaves a sharper imprint on the density profile. The redshifts at which these streams cross the halo boundary appear to be consistent with the periods of mergers for the examples shown.

Gas density profiles also suggest the presence of streams of gas being deccreted or expelled from inside the virial radius. This is particularly notorious for CL02

and CL06, and hints that dynamical interactions between clusters can also extract gaseous matter to outer radii (Cen, Pop, and Bahcall, 2014).

5.5 Understanding the angular distribution of accretion

In this section, we focus on the characterisation of the angular distribution of accreting gas. This topic has not been extensively covered in the literature, but it is of utmost interest in order to assess the influence of the clusters' environment and the complex physics of baryons on the cosmic flows. In Sec. 5.5.1, we describe our method for quantifying the angularly-resolved distribution of accretion and present and discuss some results. In Sec. 5.5.2, the validity of this approach is assessed.

5.5.1 Determination and representation of the angular distribution of accretion in simulations

A proper computation of the flux, like the one which is performed in order to solve the equations of hydrodynamics, through all the cells in the cluster boundary lacks interest for this analysis, as this would involve a tremendous computational cost without adding too much valuable physical information. Instead, in this work we suggest the computation of an estimated flux, based on the peculiar velocities and density fields at a given code output.

We assume each gas cell as a particle located at its geometrical center, with mass $\rho_B(z)(1+\delta_{\rm cell})\Delta V_{\rm cell}$ and the peculiar velocity $\mathbf{v} = a\frac{\mathrm{d}\mathbf{x}}{\mathrm{d}t}$ given by the corresponding cell-averaged velocity. All cells, regardless of the refinement level they belong to, are considered on equal footing.

For each cell, its radial comoving distance to the center of the cluster, r, and radial peculiar velocity, $v_r \equiv a\frac{\mathrm{d}r}{\mathrm{d}t}$, are computed. Let the halo be limited by a given SO boundary, at a radial comoving distance $R_{\rm bdry}$ from the centre (e.g., R_{200m}, $R_{\rm vir}$, etc.). With these data, we estimate the fluxes across the spherical boundary $R_{\rm bdry}$ according to the following rules:

- Given a cell with radial coordinate $r < R_{\rm bdry}$ (inside the spherical boundary), we mark it as an escaping cell if $r + \frac{v_r}{a}\Delta t > R_{\rm bdry}$.
- Likewise, a cell with radial coordinate $r > R_{\rm bdry}$ (outside the spherical boundary) is marked as an entering cell if $r + \frac{v_r}{a}\Delta t < R_{\rm bdry}$.

In these definitions, Δt is the time interval used in the estimation. Larger Δt increases the number of cells used to estimate the fluxes, and thus provides higher angular resolutions. However, a too long Δt would produce unreliable results, as the gas flows are not expected to be persistent on long timescales. Related to this, Sec. 5.5.2 briefly covers the validity of this approach. In our analyses, we have set Δt to be the time difference between consecutive snapshots at the moment when the fluxes are being estimated (in this simulation, this quantity takes values from $\sim 60\,$Myr to $\sim 300\,$Myr).

Once the entering and escaping cells are estimated according to our flux calculation, the angular distribution of accretion is computed by binning the complete solid angle around the cluster in the clustercentric spherical angles, ϕ and $\cos\theta$ (defined

with respect to the cartesian axes of the simulation domain). By dividing the polar direction in intervals of constant $\cos\theta$ (instead of constant θ), bins at all latitudes subtend the same solid angle. In our analyses for cluster CL01, we split the solid angle in $n_\phi \times n_\theta = 80 \times 80$ equally sized angular sectors, which yield enough resolution for our analyses. Increasing the number of bins beyond this quantity produces an excessive number of cells where no entering or escaping flows are measured, due to the approximation of cells as particles located at their geometrical center.

For each entering (escaping) cell, we assign all its mass to the bin corresponding to its angular position, yielding the distribution of accreting (deccreting) matter. Their subtraction is the net flow across the SO boundary. The resulting values can be further normalised by dividing by Δt, $R^2_{\rm bdry}$ and $\Delta\Omega = \frac{4\pi}{n_\phi n_\theta}$, in order to get the mass flux density in its proper units:

$$j_M = \frac{\Delta M}{R^2_{\rm bdry}\Delta\Omega\Delta t} \tag{5.5}$$

For the purposes of our analyses, as the main focus of this work is the study of accretion, we take the sign convention to be $j_M > 0$ when matter is infalling (being accreted).

Fig. 7 exemplifies the result of the calculations explained up to this point, for cluster CL01 at $z \approxeq 0.81$ (while it is strongly accreting mass after a major merger), with the fluxes computed at $R_{\rm vir} \approxeq 1.95\,{\rm Mpc}$. In order to produce these plots, one needs to represent positive (entering matter) and negative (escaping matter) values which span a broad range of orders of magnitude. In order to do so, we have implemented a symmetric logarithmic scale[13]. From these values, the mass flux isocontours (obtained by bilinear interpolation from the computed bins) are encoded in colour scale.

As it can be seen in the figure, accretion clearly dominates the gas mass fluxes (consistently with the fact that Γ takes a high value at this redshift). Outgoing flows of mass are restricted to small angular regions and are subdominant. The horizontal ($\cos\theta = {\rm const.}$) white lines are artifacts which arise when matter is infalling from a low level patch, which ultimately trace back to the approximation of considering all the cell's mass as a point-like particle in its center.

The angular distribution of accretion is dominated by two intense hotspots, which are located at approximately antipodal positions. These hotspots are likely to correspond to accretion through the cosmic filaments, which is assumed to be the main contribution to mass growth in clusters (Lee and Evrard, 2007; Lee et al., 2008).

[13]The symmetric logarithmic scale is a transformation of the data which allows the representation of a variable which spans several orders of magnitude and can be both positive and negative. The basic underlying idea of our particular implementation relies on mapping any interval $[-x_{\rm max}, x_{\rm max}]$ to the interval $[-1, 1]$ by performing the following continuous transformation:

$$x \mapsto f(x) = \begin{cases} {\rm sign}(x)\left[1 + \frac{1-a}{\alpha}\log_{10}\left(\frac{x}{x_{\rm max}}\right)\right], & \frac{|x|}{x_{\rm max}} \geq 10^{-\alpha} \\ \frac{a}{10^{-\alpha}x_{\rm max}}x, & \frac{|x|}{x_{\rm max}} \leq 10^{-\alpha} \end{cases} \tag{5.6}$$

The parameter $x_{\rm max}$ controls the maximum of the scale, α gives the dynamical range of the representation (the number of orders of magnitude represented in logarithmic scale) and $a = f\left(10^{-\alpha}x_{\rm max}\right)$ represents the visual extent of the linear scale. For example, in the plot shown in Fig. 7 we have chosen $\alpha = 3$, $a = 1/3$.

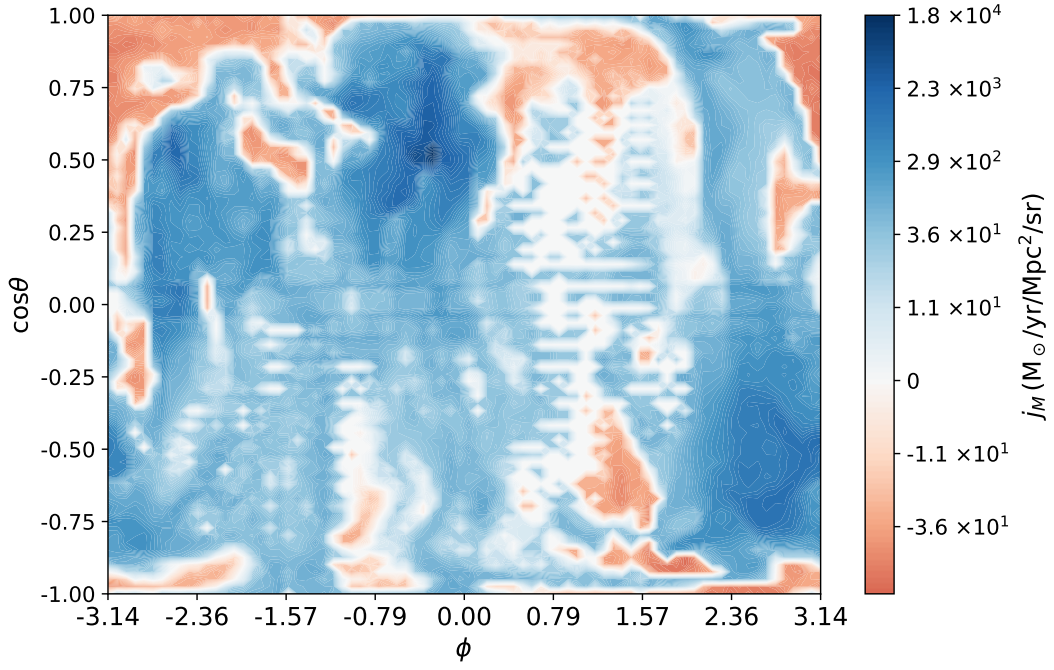

FIGURE 7: Angular distribution (with the z-axis of the domain box as the polar axis) of the estimated mass fluxes through the $r = R_{\rm vir}$ surface, for the cluster CL01 at $z \approxeq 0.81$. The plot has been produced with $n_\phi \times n_\theta = 80^2$ bins covering the 4π sr around the cluster, and using $\alpha = 3$, $a = 1/3$ for the representation. Two accretion hotspots in approximately antipodal positions dominate the infall of mass. The white, $\cos\theta = $ const. lines correspond to artifacts due to the lack of resolution in a given direction (i.e., matter infalling from a low AMR level patch).

Hereon, we will refer to this component as the *filamentary component*. Besides this filamentary component, a more *quiescent* contribution is present in nearly all directions. However, far from being isotropic, the flows have intricate structures. This complexity likely emerges from the interaction with the surroundings, and need further investigation in order to make quantitative predictions.

Although we do not explore it in the present manuscript due to the limited space, it can be seen that the filamentary component is, indeed, tightly aligned with the major axis of the total mass distribution, and it is the dominant contribution to the mass inflows throughout the cluster evolution, typically accounting for more than 50% of the accreted mass. Besides, it is worth mentioning that this method can be easily extended to quantify, not only the mass flows, but also thermodynamical properties of the accreted gas, like its temperature or entropy; or any other quantity which can be derived from the simulation outputs.

5.5.2 Validity of the approximation. Persistence of the flows.

The procedure proposed above relies on the implicit assumption that gas velocities measured at one code output are persistent during the time interval, Δt, used to estimate which gas cells enter or leave the spherical volume. In this section, we briefly

argue that this approximation is, indeed, applicable to our system, thus justifying the validity of the method.

The basic scheme of the performed test consists on the comparison of the radial velocity dispersion, σ_r, with the radial velocity, v_r. For each cell which the method described in Sec. 5.5.1 marks as entering cells, we compute its total and radial velocity dispersions as the standard deviation of such quantities in the neighbouring $5 \times 5 \times 5$ cells. Such analysis yields the following conclusions:

- The gas flows are eminently radial. The mean radial projection of the velocity of the entering cells has magnitudes $0.8 \lesssim |v_r|/v \lesssim 0.9$ for all code outputs.
- The radial velocity dispersion is typically consistent, only slightly above the isotropic value, $\sigma_r^{\rm iso} = \frac{\sigma_v}{\sqrt{3}}$. For most of the code outputs, $\frac{\sigma_r}{\sigma_r^{\rm iso}} \sim 1 - 1.1$. Having velocity dispersions near the isotropic value but much higher mean radial velocities, the relative velocity dispersion in the radial direction $\sigma_r/|v_r|$ is much smaller than in the directions tangential to the flow.
- Indeed, $|v_r|/\sigma_r$ takes mean values between 10 and 40. This high value means that, in the neighbourhood of a cell, radial gas flows are spatially coherent.

As a result of the velocities being mainly radial and the relative radial velocity dispersion being small, one should expect the shear forces between neighbouring cells to be small in the radial direction. Therefore, turbulence is not expected to have a severe impact on the overall effect of radial flows, and these can be assumed to be persistent between consecutive code outputs. Nevertheless, as our analysis has considered the mean of radial velocities, velocity dispersions, etc. across all entering cells, this does not necessarily mean that, locally, turbulence can be relevant on the radial flows in small angular regions. This would have the effect of introducing noise into our flux maps.

This simple analysis does not take into account any timescale of the variation of the computed fluxes. The timescale can be regarded as sufficiently small for our estimation of the fluxes to be valid if the angular distributions for consecutive code outputs are resemblant, i.e., they show the same structures and temporal changes are gradual. Indeed, running the same test displayed in Fig. 7 for all the code outputs from $z = 1.5$ to $z = 0$ confirms this hypothesis.

6 | Summary, Conclusions and Outlook

In this work, we have aimed to characterise the inflows of matter onto the largest virialised objects in the Universe at the present time, galaxy clusters. In order to perform such analyses, we have presented the results of a hydrodynamic+N-Body, Eulerian AMR cosmological simulation on a 40 Mpc comoving side box around a central, massive cluster. Besides the central object, several less-massive clusters and groups are also present in the simulation domain, which have turned to be useful in order to assess the differences between more massive and less massive systems. In addition to gravity and hydrodynamics, the simulation also accounts for several non-gravitational processes.

In Sec. 5.2.2, several ways of quantifying the MAR of a cluster found in the recent bibliography have been described, and the definition used through this work has been motivated. This has allowed us to study the MAH of each of the material components of the clusters in our sample, thus enabling a comparison between the intrinsically different behaviour of the collisional and collisionless components. The determinations of radii and enclosed mass taken in this work rely on the SO definitions. A possible continuation to this work could be accounting for the differences in the MAR when measured with respect to other definitions of radii, like the more dynamically-motivated splashback radius.

As a general result of our analyses, DM and baryons tend to present similar MARs in massive clusters, where the gravitational field is strong enough to capture the inflowing gas, which is pressure supported and can undergo shocks. Conversely, for low-mass objects, the different behaviour of DM and baryons is noticeable (as shown in Fig. 5b). We have suggested their lower mass (and, therefore, shallower gravitational potential well) and the interaction with other structures as a plausible explaination for their limited ability to capture gas.

In Sec. 5.3, the evolution of the DM halo has been classified into three regimes according to their merging state, in concordance with previous bibliographic works, and the behaviour of the MAR in each of the regimes has been analised. We have identified that, specially for massive clusters, high accretion rates are mantained for a long timespan after major mergers have taken place, pointing out that an important amount of mass is deposited beyond the R_{200m} boundary and is only slowly reaccreted in the following hundreds to thousands of Myr. In that respect, we also find that baryonic and DM densities in the immediate surroundings ($1 < r/R_{200m} < 1.5$) of clusters undergoing major merging events correlate quite tightly with the MAR of their respective component in the following ~ 1 Gyr, for the whole history of the clusters. However, less massive clusters do not seem to dominate as efficiently their surroundings.

The different evolution of dark and baryonic components has also been explored from the radial profiles of their corresponding densities. DM haloes interiors seem to be considerably stable, unless intense growth of mass takes place (as it has been the case for the most massive cluster in our sample). The results presented in Sec. 5.4 suggest that, while DM profiles evolution is dominated by the infall of mass,

hydrodynamical and thermodynamical effects can lead to the extraction of gas mass from the clusters.

In Sec. 5.5 we have presented a new way of analysing accretion (or mass flows, in general) through its angular distribution. The accretion picture is generally dominated by two hotspots, which are aligned with the major axis of the total mass distribution, as found by previous works in N-Body simulations. This has been associated to the matter being accreted from the cosmic filaments of the LSS. In the analyses performed on the most massive cluster, this component, coming from a small angular region, accounts for more than 50% of the mass inflow during most of the cluster evolution. The rest corresponds to a smoother component which, nevertheless, exhibits complicated spatial patterns as a result of the interaction with the environment and the complexity of the physics of baryons. As a natural extension of this analysis, which we do not cover in this text because of space limitations, the angular distribution of thermodynamical properties of the gas (their temperature or entropy), baryon fractions, etc. can also be accounted for.

The analyses in this Master's Thesis set the ground for further, short-term continuations. Still regarding accretion, besides the extensions already mentioned, other possible topics to be covered are the rotation of the different material components, the extension of these analyses to larger samples of clusters (either from `MASCLET` or from other codes, which could allow to assess the possible changes due to different numerical schemes) in order to draw statistically robust conclusions, etc.

In the mid-term future, and intimately related to accretion and strong gradients, shock waves and turbulence in galaxy clusters have been recently triggering increasing interest of the scientific community, and are also natural extension lines of this work. Last, the new version of `MASCLET` will allow to quantify the influence of magnetic fields on the studied phenomena. Covering these topics, a FPU doctoral fellowship project has been proposed, under the title *Untangling the complexity of cosmic flows in the Universe: the role of strong gradients, shock waves and turbulence.*

References

Abell, G. O. (1958). "The Distribution of Rich Clusters of Galaxies." In: *The Astrophysical Journal Supplement Series* 3, p. 211. ISSN: 0067-0049. DOI: 10.1086/190036.

Adhikari, S., Dalal, N., and Chamberlain, R. T. (2014). "Splashback in accreting dark matter halos". In: *Journal of Cosmology and Astroparticle Physics* 2014.11, p. 19. ISSN: 1475-7516. DOI: 10.1088/1475-7516/2014/11/019. arXiv: 1409.4482.

Allen, S. W., Evrard, A. E., and Mantz, A. B. (2011). "Cosmological Parameters from Observations of Galaxy Clusters". In: *Annual Review of Astronomy and Astrophysics* 49.1, pp. 409–470. ISSN: 0066-4146. DOI: 10.1146/annurev-astro-081710-102514. arXiv: 1103.4829.

Bertschinger, E. (1998). "Simulations of Structure Formation in the Universe". In: *Annual Review of Astronomy and Astrophysics* 36.1, pp. 599–654. ISSN: 0066-4146. DOI: 10.1146/annurev.astro.36.1.599.

Biffi, V. et al. (2016). "On the Nature of Hydrostatic Equilibrium in Galaxy Clusters". In: *The Astrophysical Journal* 827.2, p. 112. ISSN: 1538-4357. DOI: 10.3847/0004-637x/827/2/112. arXiv: 1606.02293.

Borgani, S. and Kravtsov, A. V. (2011). "Cosmological simulations of galaxy clusters". In: *Advanced Science Letters* 4.2, pp. 204–227. ISSN: 19366612. DOI: 10.1166/asl.2011.1209. arXiv: 0906.4370.

Brent, R. P. (1973). *Algorithms for Minimization without Derivatives*. Englewood Cliffs, New Jersey: Prentice-Hall. ISBN: 0-13-022335-2.

Bryan, G. L. and Norman, M. L. (1998). "Statistical Properties of X-Ray Clusters: Analytic and Numerical Comparisons". In: *The Astrophysical Journal* 495.1, pp. 80–99. ISSN: 0004-637X. DOI: 10.1086/305262. arXiv: astro-ph/9710107.

Cen, R., Pop, A. R., and Bahcall, N. A. (2014). "Gas Loss in Simulated Galaxies as They Fall into Clusters". In: *Proceedings of the National Academy of Sciences of the United States of America* 104.51, pp. 20167–20172. ISSN: 00278424. DOI: 10.1073/pnas.1407300111. arXiv: 1405.0537.

Chen, H. et al. (2019). "Imprints of mass accretion history on the shape of the intracluster medium and the TX-M relation". In: *Monthly Notices of the Royal Astronomical Society* 490.2, pp. 2380–2389. ISSN: 13652966. DOI: 10.1093/mnras/stz2776. arXiv: 1903.08662.

Chen, Y. et al. (2020). "Relating the structure of dark matter halos to their assembly and environment". In: arXiv: 2003.05137.

Cui, W. et al. (2016). "How does our choice of observable influence our estimation of the centre of a galaxy cluster? Insights from cosmological simulations". In: *Monthly Notices of the Royal Astronomical Society* 456.3, pp. 2566–2575. ISSN: 0035-8711. DOI: 10.1093/mnras/stv2839. arXiv: 1512.01253.

Davis, M. et al. (1985). "The evolution of large-scale structure in a universe dominated by cold dark matter". In: *The Astrophysical Journal* 292.9, pp. 371–394. ISSN: 0004-637X. DOI: 10.1086/163168.

Diemer, B. and Kravtsov, A. V. (2014). "Dependence of the outer density profiles of halos on their mass accretion rate". In: *The Astrophysical Journal* 789.1, p. 1. ISSN: 0004-637X. DOI: 10.1088/0004-637X/789/1/1. arXiv: 1401.1216.

Dolag, K. et al. (2008). "Simulation Techniques for Cosmological Simulations". In: *Space Science Reviews* 134.1-4, pp. 229–268. ISSN: 0038-6308. DOI: 10.1007/s11214-008-9316-5. arXiv: 0801.1023.

Giodini, S. et al. (2013). "Scaling relations for galaxy clusters: Properties and evolution". In: *Space Science Reviews* 177.1-4, pp. 247–282. ISSN: 00386308. DOI: 10.1007/s11214-013-9994-5. arXiv: 1305.3286.

Gunn, J. E. and Gott, J. R. I. (1972). "On the Infall of Matter Into Clusters of Galaxies and Some Effects on Their Evolution". In: *The Astrophysical Journal* 176, p. 1. ISSN: 0004-637X. DOI: 10.1086/151605.

Hamilton, J.-C. (2014). "What have we learned from observational cosmology?" In: *Studies in History and Philosophy of Science Part B: Studies in History and Philosophy of Modern Physics* 46, pp. 70–85. ISSN: 13552198. DOI: 10.1016/j.shpsb.2013.02.002. arXiv: 1304.4446.

Knebe, A. et al. (2011). "Haloes gone MAD: The Halo-Finder Comparison Project". In: *Monthly Notices of the Royal Astronomical Society* 415.3, pp. 2293–2318. DOI: 10.1111/j.1365-2966.2011.18858.x. arXiv: 1104.0949.

Kravtsov, A. V. and Borgani, S. (2012). "Formation of Galaxy Clusters". In: *Annual Review of Astronomy and Astrophysics* 50.1, pp. 353–409. ISSN: 0066-4146. DOI: 10.1146/annurev-astro-081811-125502. arXiv: 1205.5556.

Lacey, C. and Cole, S. (1994). "Merger rates in hierarchical models of galaxy formation – II. Comparison with N-body simulations". In: *Monthly Notices of the Royal Astronomical Society* 271.3, pp. 676–692. ISSN: 0035-8711. DOI: 10.1093/mnras/271.3.676.

Landau, L. and Lifshitz, E. (1987). *Course of Theoretical Physics, vol. 6, Fluid Mechanics*. 2nd. Oxford: Butterworth-Heinemann. ISBN: 978-0750627672.

Lau, E. T. et al. (2014). "Mass Accretion and its Effects on the Self-Similarity of Gas Profiles in the Outskirts of Galaxy Clusters". In: *The Astrophysical Journal* 806.1, p. 68. ISSN: 1538-4357. DOI: 10.1088/0004-637X/806/1/68. arXiv: 1411.5361.

Lee, J. and Evrard, A. E. (2007). "Cluster-Supercluster Alignments". In: *The Astrophysical Journal* 657.1, pp. 30–36. ISSN: 0004-637X. DOI: 10.1086/511003. arXiv: astro-ph/0608685.

Lee, J. et al. (2008). "Quantifying the cosmic web - I. the large-scale halo ellipticity-ellipticity and ellipticity-direction correlations". In: *Monthly Notices of the Royal Astronomical Society* 389.3, pp. 1266–1274. ISSN: 00358711. DOI: 10.1111/j.1365-2966.2008.13624.x. arXiv: 0709.1106.

Liddle, A. R. (2004). "How many cosmological parameters?" In: *Monthly Notices of the Royal Astronomical Society* 351.3, pp. L49–L53. ISSN: 00358711. DOI: 10.1111/j.1365-2966.2004.08033.x. arXiv: astro-ph/0401198.

More, S., Diemer, B., and Kravtsov, A. V. (2015). "The splashback radius as a physical halo boundary and the growth of halo mass". In: *The Astrophysical Journal* 810.1, p. 36. ISSN: 1538-4357. DOI: 10.1088/0004-637X/810/1/36. arXiv: 1504.05591.

Navarro, J. F., Frenk, C. S., and White, S. D. M. (1997). "A Universal Density Profile from Hierarchical Clustering". In: *The Astrophysical Journal* 490.2, pp. 493–508. ISSN: 0004-637X. DOI: 10.1086/304888. arXiv: astro-ph/9611107.

Ntelis, P. (2016). "The Homogeneity Scale of the Universe". In: arXiv: 1607.03418.

Peebles, P. (1980). *The Large-Scale Structure of the Universe*. Princeton University Press. ISBN: 9780691082400.

Peebles, P. (1993). *Principles of Physical Cosmology*. Princeton University Press. ISBN: 9780691019338.

Planck Collaboration (2018). "Planck 2018 results. VI. Cosmological parameters". In: arXiv: 1807.06209.

Planelles, S. (2011). "New Insights into Galaxy Clusters: from Simulations to Observations". PhD thesis. Universitat de València.

Planelles, S. and Quilis, V. (2009). "Galaxy cluster mergers". In: *Monthly Notices of the Royal Astronomical Society* 399.1, pp. 410–424. ISSN: 00358711. DOI: 10.1111/j.1365-2966.2009.15290.x. arXiv: 0906.4024.

Planelles, S. and Quilis, V. (2010). "ASOHF: a new adaptive spherical overdensity halo finder". In: *Astronomy and Astrophysics* 519, A94. ISSN: 0004-6361. DOI: 10.1051/0004-6361/201014214. arXiv: 1006.3205.

Planelles, S. and Quilis, V. (2013). "Cosmological shock waves: Clues to the formation history of haloes". In: *Monthly Notices of the Royal Astronomical Society* 428.2, pp. 1643–1655. ISSN: 00358711. DOI: 10.1093/mnras/sts142. arXiv: 1210.1369.

Planelles, S., Schleicher, D. R. G., and Bykov, A. M. (2015). "Large-Scale Structure Formation: From the First Non-linear Objects to Massive Galaxy Clusters". In: *Space Science Reviews* 188.1-4, pp. 93–139. ISSN: 0038-6308. DOI: 10.1007/s11214-014-0045-7. arXiv: 1404.3956.

Planelles, S. et al. (2013). "Baryon census in hydrodynamical simulations of galaxy clusters". In: *Monthly Notices of the Royal Astronomical Society* 431.2, pp. 1487–1502. ISSN: 1365-2966. DOI: 10.1093/mnras/stt265. arXiv: 1209.5058.

Planelles, S. et al. (2018). "Multiwavelength mock observations of the WHIM in a simulated galaxy cluster". In: *Monthly Notices of the Royal Astronomical Society* 476.4, pp. 4629–4648. ISSN: 13652966. DOI: 10.1093/mnras/sty527.

Press, W. H. and Teukolsky, S. A. (1990). "Savitzky-Golay Smoothing Filters". In: *Computers in Physics* 4.6, p. 669. ISSN: 08941866. DOI: 10.1063/1.4822961.

Quilis, V. (2004). "A new multidimensional adaptive mesh refinement hydro + gravity cosmological code". In: *Monthly Notices of the Royal Astronomical Society* 352.4, pp. 1426–1438. ISSN: 00358711. DOI: 10.1111/j.1365-2966.2004.08040.x. arXiv: astro-ph/0405389.

Quilis, V., Ibáñez, J. M., and Sáez, D. (1994). "Modern high-resolution shock-capturing methods for structure evolution in cosmology". In: *Astronomy & Astrophysics* 286, pp. 1–16.

Quilis, V., Ibáñez, J. M., and Sáez, D. (1996). "A Multidimensional Hydrodynamic Code for Structure Evolution in Cosmology". In: *The Astrophysical Journal* 469, p. 11. ISSN: 0004-637X. DOI: 10.1086/177753. arXiv: astro-ph/9604037.

Quilis, V., Martí, J.-M., and Planelles, S. (2020). "Cosmic magnetic fields with MASCLET: an application to galaxy clusters". In: *Monthly Notices of the Royal Astronomical Society* 13.March, pp. 2706–2717. ISSN: 0035-8711. DOI: 10.1093/mnras/staa877. arXiv: 2003.12306.

Quilis, V., Planelles, S., and Ricciardelli, E. (2017). "Is ram-pressure stripping an efficient mechanism to remove gas in galaxies?" In: *Monthly Notices of the Royal Astronomical Society* 469.1, pp. 80–94. ISSN: 0035-8711. DOI: 10.1093/mnras/stx770. arXiv: 1703.09446.

Savitzky, A. and Golay, M. J. E. (1964). "Smoothing and Differentiation of Data by Simplified Least Squares Procedures." In: *Analytical Chemistry* 36.8, pp. 1627–1639. ISSN: 0003-2700. DOI: 10.1021/ac60214a047.

Tanabashi, M. et al. (2018). "Review of Particle Physics". In: *Physical Review D* 98.3, p. 030001. ISSN: 2470-0010. DOI: 10.1103/PhysRevD.98.030001.

Theuns, T. (2016). *Lecture notes in Physical Cosmology*. URL: http://www.icc.dur.ac.uk/~tt/teaching.html.

Tormen, G., Moscardini, L., and Yoshida, N. (2004). "Properties of cluster satellites in hydrodynamical simulations". In: *Monthly Notices of the Royal Astronomical Society* 350.4, pp. 1397–1408. ISSN: 00358711. DOI: 10.1111/j.1365-2966.2004.07736.x. arXiv: astro-ph/0304375.

Voit, G. M. (2005). "Tracing cosmic evolution with clusters of galaxies". In: *Reviews of Modern Physics* 77.1, pp. 207–258. ISSN: 00346861. DOI: 10.1103/RevModPhys.77.207. arXiv: astro-ph/0410173.

Walker, S. et al. (2019). "The Physics of Galaxy Cluster Outskirts". In: *Space Science Reviews* 215.1. ISSN: 15729672. DOI: 10.1007/s11214-018-0572-8. arXiv: 1810.00890.

Zwicky, F. (1933). "Die Rotverschiebung von extragalaktischen Nebeln". In: *Helvetica Physica Acta* 6, pp. 110–127.